Title

XFEL serial crystallography reveals the room temperature structure of methyl-coenzyme M reductase

Authors

Ohmer, Christopher J

Dasgupta, Medhanjali

Patwardhan, Anjali

et al.

Publication Date

2022-05-01

DOI

10.1016/j.jinorgbio.2022.111768

Peer reviewed

Journal of Inorganic Biochemistry 230 (2022) 111768

Contents lists available at ScienceDirect

Journal of Inorganic Biochemistry

journal homepage: www.elsevier.com/locate/jinorgbio

XFEL serial crystallography reveals the room temperature structure of methyl-coenzyme M reductase

Christopher J. Ohmer [a,1], Medhanjali Dasgupta [b,1], Anjali Patwardhan [a], Isabel Bogacz [b], Corey Kaminsky [b], Margaret D. Doyle [b], Percival Yang-Ting Chen [c,2], Stephen M. Keable [b], Hiroki Makita [b], Philipp S. Simon [b], Ramzi Massad [b,i], Thomas Fransson [d], Ruchira Chatterjee [b], Asmit Bhowmick [b], Daniel W. Paley [b], Nigel W. Moriarty [b], Aaron S. Brewster [b], Leland B. Gee [e], Roberto Alonso-Mori [e], Frank Moss [e], Franklin D. Fuller [e], Alexander Batyuk [e], Nicholas K. Sauter [b], Uwe Bergmann [f], Catherine L. Drennan [c,g,h], Vittal K. Yachandra [b], Junko Yano [b,*], Jan F. Kern [b,*], Stephen W. Ragsdale [a,*]

[a] Department of Biological Chemistry, University of Michigan Medical School, 1150 W. Medical Center Dr., 5200 MSRBIII, Ann Arbor, MI 48109-0606, USA
[b] Molecular Biophysics and Integrated Bioimaging Division, Lawrence Berkeley National Laboratory, Berkeley, CA 94720, USA
[c] Department of Chemistry, Massachusetts Institute of Technology, 77 Massachusetts Avenue, Cambridge, MA 02139, USA
[d] Department of Theoretical Chemistry and Biology, KTH Royal Institute of Technology, Stockholm, Sweden
[e] LCLS, SLAC National Accelerator Laboratory, Menlo Park, CA 94025, USA
[f] Department of Physics, University of Wisconsin-Madison, Madison, WI 53706, USA
[g] Department of Biology and the Howard Hughes Medical Institute, Massachusetts Institute of Technology, 77 Massachusetts Avenue, Cambridge, MA 02139, USA
[h] Canadian Institute for Advanced Research, Bio-inspired Solar Energy Program, Toronto, ON M5G 1M1, Canada
[i] Department of Chemistry and Biochemistry, University of California, Los Angeles, CA 90095, USA

ARTICLE INFO

Keywords:
Methanogens
Nickel
X-ray Free-Electron Laser (XFEL)
Serial femtosecond crystallography (SFX)
X-ray Diffraction (XRD)
X-ray Emission Spectroscopy (XES)

ABSTRACT

Methyl-Coenzyme M Reductase (MCR) catalyzes the biosynthesis of methane in methanogenic archaea, using a catalytic Ni-centered Cofactor F430 in its active site. It also catalyzes the reverse reaction, that is, the anaerobic activation and oxidation, including the cleavage of the C—H bond in methane. Because methanogenesis is the major source of methane on earth, understanding the reaction mechanism of this enzyme can have massive implications in global energy balances. While recent publications have proposed a radical-based catalytic mechanism as well as novel sulfonate-based binding modes of MCR for its native substrates, the structure of the active state of MCR, as well as a complete characterization of the reaction, remain elusive. Previous attempts to structurally characterize the active MCR-Ni(I) state have been unsuccessful due to oxidation of the redox- sensitive catalytic Ni center. Further, while many cryo structures of the inactive Ni(II)-enzyme in various substrates-bound forms have been published, no room temperature structures have been reported, and the structure and mechanism of MCR under physiologically relevant conditions is not known. In this study, we report the first room temperature structure of the MCRred1-silent Ni(II) form using an X-ray Free-Electron Laser (XFEL), with simultaneous X-ray Emission Spectroscopy (XES) and X-ray Diffraction (XRD) data collection. In celebration of the seminal contributions of inorganic chemist Dick Holm to our understanding of nickel-based catalysis, we are honored to announce our findings in this special issue dedicated to this remarkable pioneer of bioinorganic chemistry.

Abbreviations: MCR, Methyl-Coenzyme M Reductase; CH_3-SCoM, Methyl-Coenzyme M; DOT, Drop-On-Tape; ECR, Ethyl-coenzyme M Reductase; HSCoB, Coenzyme B; LCLS, Linac Coherent Light Source; RT, Room Temperature; XES, X-ray Emission Spectroscopy; XFEL, X-ray Free Electron Laser; XRD, X-ray Diffraction.

* Corresponding authors.
E-mail addresses: jyano@lbl.gov (J. Yano), jfkern@lbl.gov (J.F. Kern), sragsdal@umich.edu (S.W. Ragsdale).

[1] These authors contributed equally.

[2] Current address: Morphic Therapeutic, 35 Gatehouse Drive, A2, Waltham, MA 02451, USA.

https://doi.org/10.1016/j.jinorgbio.2022.111768
Received 10 November 2021; Received in revised form 10 February 2022; Accepted 10 February 2022
Available online 17 February 2022

1. Introduction

Methane is ~25 times more potent as a greenhouse gas compared to carbon dioxide, and it has been estimated that it has contributed to about 20% of earth's warming since the industrial revolution [1]. Methanogenic microbes are responsible for producing about 100 billion tons of methane per year [2]. Although methanogenesis is the primary source of methane in the atmosphere, anaerobic methane oxidizing archaea found in marine ecosystems and aerated and dry soils use methane as an energy source [3]. Additionally, methane oxidation via hydroxyl radicals is the primary sink for atmospheric methane [4]. This generation and depletion of methane is a major contributor to the global carbon cycle and is critical for maintaining the earth's temperatures. Within the last 200 years, the concentration of methane in the atmosphere has more than doubled due to increased agricultural ruminants, mining of natural gases, and landfill seeps [5,6]. The global carbon cycle has been thrown out of sustainable equilibrium causing extreme droughts throughout Africa and the Mediterranean, heat, and precipitation [7]. Despite its global warming effect, methane, having the highest energy content of any carbon-based fuel, is very important for energy production, and accounts for 22% of U.S. energy consumption, with half of homes using natural gas as their heating fuel. Therefore, understanding the mechanism and energetics of methane formation will enable more efficient biofuel production, providing us with a more sustainable source of energy while decreasing our dependence on fossil fuels and natural gas.

The nickel enzyme Methyl Coenzyme M Reductase (MCR) is responsible for the synthesis of methane in methanogens. MCR catalyzes the conversion of methyl-coenzyme M (CH_3-SCoM) and coenzyme B (HSCoB) to the heterodisulfide CoMSSCoB and methane [8]. Interestingly, MCR can also catalyze the reverse reaction, that is, the anaerobic oxidation of methane in a syntrophic process coupled to sulfate reduction [9]. This activation and subsequent cleavage of the very strong alkane C—H bond in methane occurs at its active site Ni(I)-F430 cofactor without utilizing any reactive oxygen species. Moreover, the reverse reaction of methane oxidation catalyzed by MCR in anaerobic methane oxidizing archaea (ANME) is one of the major biological sinks for atmospheric methane [10]. The specifics of the mechanism of MCR catalysis, however, still remain elusive.

Thus, a complete understanding of the structure and any potential physiologically relevant conformational dynamics in MCR is important. A variety of catalytic intermediates, including the formation of a Ni-alkyl intermediate shown in Fig. 1A, have been proposed over the years based on various biochemical investigations and computational studies [11]. On the other hand, computational work proposed that the Ni-alkyl mechanism is too high in energy and provided evidence for a methyl radical-based mechanism of methane formation [12]. In 2016, based on computational, spectroscopic, and rapid kinetic studies, Wongnate et al. provided evidence supporting the formation of a methyl radical and disfavoring the Ni-alkyl mechanism [13].

The binding mode of substrates in all proposed mechanisms has been mostly based on their orientations within a 50 Å substrate channel as observed in the Ni(II) crystal structures [14–18]. As described in the canonical mechanism of Fig. 1B, it is proposed that CH_3-SCoM binds to Ni(I) through a Ni—S interaction with HSCoB tethered above the F430 catalytic center. In Step 1, homolytic cleavage of the S—C bond of CH_3-SCoM results in a methyl radical. The methyl radical then abstracts a hydrogen atom from HSCoB, forming methane and a CoBS radical. In Step 3, the CoBS radical then reacts with the Ni thiolate complex forming a heterodisulfide anion radical intermediate, which transfers an electron into the Ni(II) to form CoBSSCoM and regenerate the active-Ni (I) state. In these mechanistic proposals, the CoBS radical must overcome an apparent 6.4 Å gap, as seen in various crystal structures of the Ni(II)-MCR-substrate-complex, to form the S—S bond of CoMSSCoB. Recent studies by our group have challenged the canonical binding mode of MCR [19]. Near-infrared, X-ray absorption spectroscopy, and electron paramagnetic resonance (EPR) studies have described a Ni-sulfonate coordination of the sulfonate group of CH_3-SCoM, shown in Fig. 1, rather than the thiolate as previously suggested [15]. This binding mode places the two sulfurs (of SCoB and SCoM) within bonding distance. However, it implies a long-distance electron transfer mechanism from Ni(I) to cleave the C—S bond of CH_3-SCoM.

Further studies are required to discriminate between the various proposed mechanisms and gain insight into how the C—H bond of

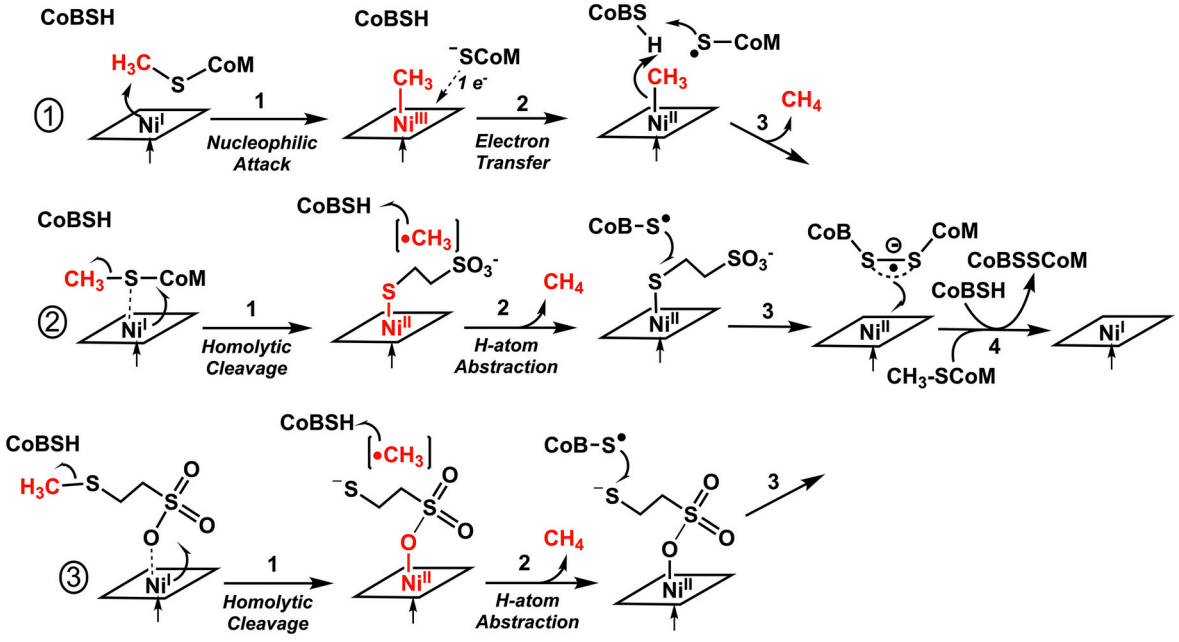

Fig. 1. Proposed organometallic versus radical mechanisms MCR-catalyzed methane formation. (A) Organometallic mechanism involving nucleophilic attack on methyl-CoM to form a Ni(III)-methyl intermediate (B) Ni(I) promoted homolysis of the methyl-S bond of methyl-CoM to form a methyl radical and Ni(II)-thiolate of CoM. (C) Ni(I) promoted homolysis of the methyl-thioether bond of methyl-SCoM bound through long-range electron transfer from a Ni-sulfonate bond to generate a methyl radical and Ni(II)-sulfonate (as proposed by Patwardhan et al. [19]).

methane is enzymatically formed and activated. A critical limitation to that is the challenge of crystallizing MCR in its active reduced Ni(I) form. Due to the extremely low Ni(II)/(I) redox potential, the Ni(I) form is highly sensitive to oxidation during handling [17], even under highly anoxic conditions; These are significant challenges to structural elucidation of the active form of MCR. Thus, all structures of MCR so far have captured the inactive Ni(II) forms, MCRred1-silent and MCRox1-silent, formed upon air exposure from MCRred1 and MCRox1, respectively [16]. Even dark green MCRred1 crystals grown and harvested within an anaerobic chamber at <1 ppm O_2 undergo oxidation to the yellow MCRred1-silent state by exposure to even small amounts of ambient oxygen present during X-ray data collection [17]. Moreover, no room-temperature structure currently exists for any state of MCR. Cryo-crystallography has yielded many MCR structures but it has some limitations. Damage to the crystals from rapid freezing, the need for optimization of cryoprotectants, and ice ring interference are all problems that must be overcome with cryo structures [20]. Most importantly, cryo-crystallography provides limited insight into physiologically relevant protein dynamics. Room temperature (RT) crystallography gives us the opportunity to overcome this issue and study MCR conformational dynamics at more physiologically relevant conditions [21].

This present study provides a glimpse of the first room-temperature crystal structure of MCR. This structure was obtained using the X-ray Free Electron Laser (XFEL) at Linac Coherent Light Source (LCLS) and describes the Ni(II)-MCRred1-silent state of the well-studied MCR from *Methanothermobacter marburgensis*. The rationale for pursuing XFEL rather than synchrotron measurements for this room-temperature structure of MCR is based on the limitations of cryo structures described above. For example, the S—C bond in CH_3-SCoM has been suggested to break due to radiation-induced damage during data collection [16]. This may explain why CH_3-SCoM has not been observed in any synchrotron-based crystal structures [14–18]. In this report of the room-temperature crystal structure of MCR, we aim to provide a snapshot into its active site architecture and reveal potentially functionally relevant conformational dynamics. We also present a structure of MCR Ni(II) pressurized with xenon gas in an attempt to map gas channels within this fascinating enzyme, with the continuing goal of using these methods to map potentially important gas channels in the active Ni(I) MCR enzyme undergoing catalysis.

2. Materials and methods

2.1. Purification and crystallization of MCRred1-silent

MCRred1 from *M. marburgensis* (catalog OCM82) was purified and handled in an anaerobic chamber (Vacuum Atmospheres, Inc. or MBRAUN) containing <1 ppm of O_2, as previously described [17,19]. We removed the Ni(I)-enzyme from the chamber to convert the enzyme to the inactive Ni(II)-state, also known as MCRred1-silent. To be noted, this is different from the MCRox1-silent state where MCRox1 is air exposed [16]. UV–Vis spectroscopy following purification and oxidation of the MCR protein shows the catalytic Ni to be in the +2 oxidation state (SI Fig. 1), indicating conversion to the MCRred1-silent form.

The concentration of MCRred1-silent used for crystallization was quantified using UV–Vis spectrophotometry with extinction coefficients of 22.0 and 12.7 mM^{-1} cm^{-1} at 420 and 385 nm, respectively, using a multi-wavelength calculation as previously described [22]. All crystallization of MCRred1-silent was carried out at a concentration of 150 mM (40 mg/mL) in 50 mM Tris, pH 7.6. The crystallization buffer used in both crystal drops and the well reservoir is composed of 18% PEG 400, 150 mM magnesium acetate hexahydrate, and 100 mM HEPES Sodium, pH 7.5. Hanging drop vapor diffusion was used with 1:1 ratios of protein solution and crystallization buffer, respectively, to produce crystallization solutions ranging from 2 to 10 μL with a well solution containing 0.5 mL crystallization buffer. Crystals of MCRred1-silent grew overnight, but the crystals were too large (~100–200 μm sized) to be appropriate for XFEL analysis. Crushing big MCR crystals by vortexing for 5 min with a Teflon bead (0.5 mm) fragmented the crystals but damaged diffraction quality which was demonstrated during screening at the Advanced Light Source (ALS, beamline 8.2.1), Berkeley. We grew slightly smaller MCRred1-silent crystals (40–80 μm) by adjusting the seed stock concentration in our hanging drop trials and used these microcrystals for our RT XFEL measurements. They belong to space group P21 (a = 83.08 ± 0.09 Å, b = 119.78 ± 0.16 Å, c = 123.21 ± 0.15 Å, α = 90°, β = 91.7°, γ = 90°) with two MCR dimers per asymmetric unit as reported previously [17] (Fig. 2).

2.2. Sample delivery, X-ray Diffraction (XRD) and X-ray Emission Spectroscopy (XES) data collection at LCLS

XFEL diffraction data were collected at the Macromolecular Femtosecond Crystallography (MFX) instrument of LCLS, (SLAC National Accelerator Lab, Menlo Park, CA) [23] at 300 K on a RAYONIX MX340-HS CCD detector, using the previously established Drop-On-Tape (DOT) [24] approach (SI Fig. 2). The X-ray beam photon energy was 9.5 keV with a pulse energy of 1 mJ, a pulse length of 35 fs and a beam size on the sample of 4 μm × 4 μm (Full Width Half Max, FWHM). Data collection statistics are available in SI Table 1. X-ray emission data were collected in tandem with diffraction data using a multicrystal wavelength-dispersive hard X-ray spectrometer based on the von Hamos geometry [25]. Due to the change of polarization direction of the hard X-ray undulator of LCLS our previously used setup [24,25] was modified to place the analyzer crystals above the X-ray interaction point and the position sensitive detector at 90 degrees from the beam direction in the horizontal plane. An array of three Si(620) analyzer crystals was placed 250 mm above the interaction point with the center of the crystals at 74.80 degrees respect to the interaction point, collecting both Ni Kα lines on an ePix 100 detector with its center located 136 mm side wise of the X-ray interaction point (SI Fig. 2). To calibrate the spectrometer geometry, spectra from $[Ni(H2O)6]^{2+}$ were collected and compared to a synchrotron reference. The XES data was also pedestal corrected to account for differences in noise of the detector pixels.

2.3. XRD data reduction, processing, and refinement

The collected dataset was reduced and processed using *cctbx.xfel* and DIALS [26,27]. We performed joint refinement of the crystal models against the detector position for each batch to account for small time-dependent variations in detector position [27]. We also corrected for the Kapton tape shadow as in [24]. Data were scaled and merged to 1.9 Å based on previously established resolution cutoff criteria (~10× multiplicity, where the values of I/σ(I) do not uniformly decrease any more [24], and where cc1/2 values stop decreasing monotonically [28], indicating no useful information is contained in resolution shells beyond that point), using *cctbx.xfel.merge* with errors determined by the ev11 method [29]. Data statistics are available in SI Table 1. Structure determination was done using Phenix [30] starting with molecular replacement using the model PDB ID: 3M1V [17] as the reference model [31]. For all subsequent refinements with Phenix, we turned off automatic linking within the chain, as well as NCS restraints, and instead defined the interactions between the Ni-OE1(Q147) and Ni-S1(CoM) by supplying custom coordination restraints as parameter (phil) files. We used Coot [32] for model building with multiple iterations of refinement using phenix.refine [30,33,34] with the aforementioned settings. Comparisons of the cryogenic MCRred1 models with the room temperature model were performed using the SSM function in Coot [35]. All figures for this paper were generated using Chimera [36] and Chimera-X [37].

2.4. Xe-pressurized cryo-crystallography

MCR was crystallized using the sitting drop crystallization method in an In Situ-1 Crystallization Plate (MiTeGen) under aerobic conditions in

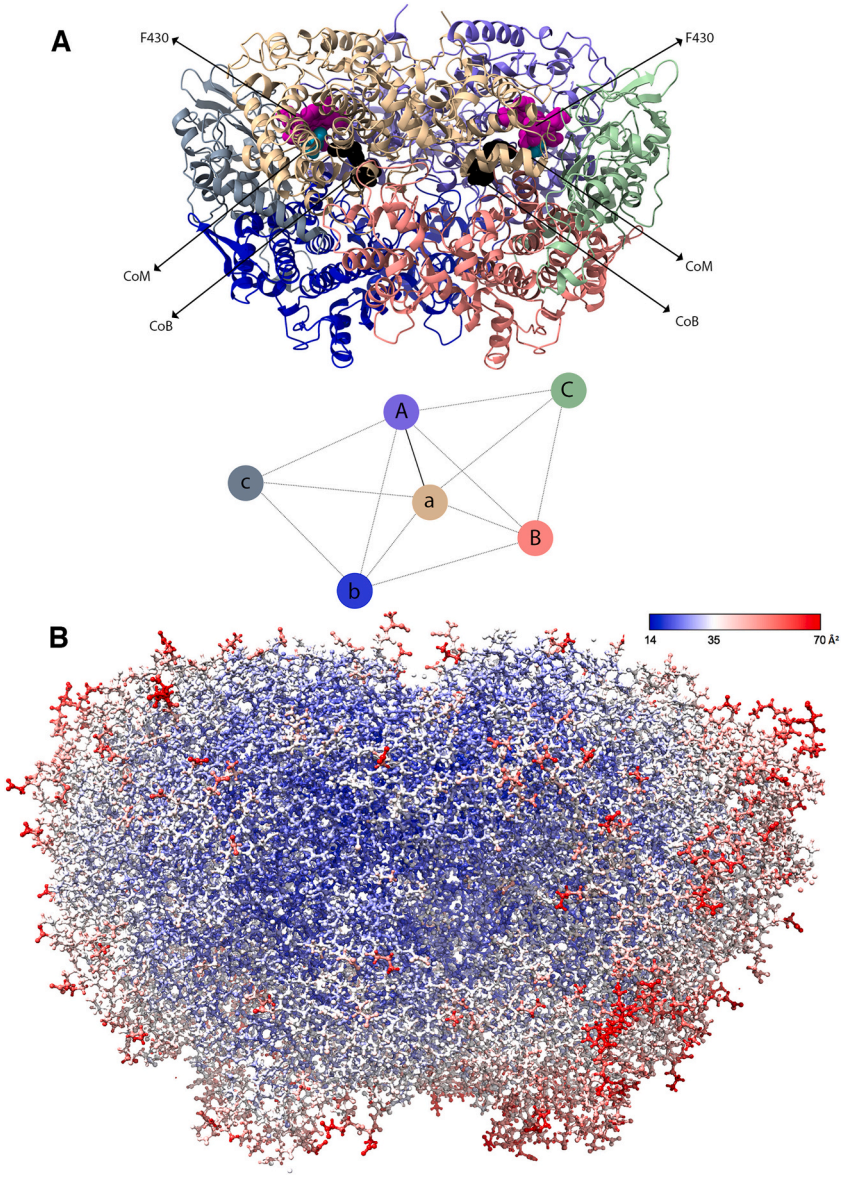

Fig. 2. A. Room Temperature structure of MCRred1-silent (Top): The global structure of MCRred1-silent at room temperature shows two trimers per asymmetric unit; trimer 1 is comprised of chains A (Purple), B (Salmon), C (Green) and trimer 2 is comprised of chains a (Tan), b (Blue), c (Grey). CoM (red with green outline), CoB (Black) and Ni—F430 (Magenta) are shown as sphere representations and are labeled. (Bottom) shows the 12 contacts between the 6 chains. (B) B factor analysis across the entire structure of MCRred1-silent shows overall similar B factors across both trimers (low B factors towards the core of the protein and higher B factors towards the surfaces, as expected). Figure made with Chimera-X(1.3). (For interpretation of the references to colour in this figure legend, the reader is referred to the web version of this article.)

an MBraun Chamber at room temperature. 1 μL of 24 mg/mL MCR was mixed with 1 μL of well solution (27% (*w/v*) PEG400, 0.18 M magnesium acetate, 0.25 M sodium chloride, and 0.10 M HEPES pH 7.5) to make a 2-μL sitting drop in a sealed well with 30 μL well solution. Yellowish green rod MCR crystals grew in two to four hrs. The entire crystallization plate was shipped to Advanced Light Source Beamline 8.2.2 for Xe- pressurization and data collection. The crystals used to determine Xe-derivatized structure were transferred from the sitting drop into 2–5 μL of paraffin oil briefly and then sealed in a steel chamber pressurized with xenon at 180 psi for 10 mins. The Xe-derivatized crystals were flash-cooled in liquid nitrogen for data collection immediately. Data were collected at ALS 8.2.2 on an ADSC Q315R CCD detector using the inverse beam method with wavelength at 1.5498 Å. The dataset was indexed and scaled in HKL2000 [38] with Bijvoet pairs treated independently. cc1/2 ~ 0.75 was used as the high-solution cutoff criteria. Data statistics are listed in SI Table 2. The structure of Xe-derivatized MCR was determined to 2.5-Å resolution by rigid body refinement from previously published MCR structure (PDB ID: 3M1V) using Phenix.refine [33]. The model contains a dimer of heterotrimers in the asymmetric unit (Fig. 2). The atomic coordinates and B-factors were iteratively refined in Phenix Refine with manual adjustment of the model in Coot [32,33,35]. Two-fold non-crystallographic symmetry (NCS) restraints were used throughout refinement. Water molecules were added manually using Fo-Fc density contoured to 3.0σ as criteria. Xenon sites were assigned using anomalous difference density contoured to 5.0σ as criteria. Occupancies of xenon atoms were adjusted such that the B factors of xenon atoms are similar to atoms nearby. Restraints for cofactors and modified amino acids were generated with Phenix.eLBOW [33]. A composite-omit electron density map was calculated using Phenix to verify the model. The refinement statistics are listed in SI Table 2. Software used to process Xe- derivatized MCR dataset was provided by SBGrid [39].

2.5. Identification of potential "gas tunnels" in MCRred1-silent and its ethane-oxidizing homolog ethyl-coenzyme M reductase (ECR)

Caver [40] was used to identify potential tunnels in our RT MCRred1-silent structure. Key amino acid residues were identified in our structure by a sequence alignment with identified ECR (7B1S) residues around the gas tunnel via Clustal-W [41].

3. Results

3.1. Comparison of the first XFEL structure of MCRred1-silent at 1.9 Å resolution with cryogenic structures

We collected a 1.9 Å resolution X-ray Diffraction dataset for the (Ni-II) MCRred1-silent state using microcrystals at the X-ray Free-Electron Laser (XFEL) source at LCLS. Although several cryo structures of MCRred1-silent currently exist, this new structure is important as it provides us with the exciting opportunity to study physiologically relevant MCR dynamics and/or any functionally significant conformational shifts that are permitted only at temperatures above freezing. In our presented structure, MCRred1-silent exists as a dimer of trimers (Chains A, B, C and a, b, and c) with 12 contacts across the six chains (Fig. 2), forming the 50 Å long substrate tunnel leading to the catalytic Ni—F430 (SI Fig. 3B). Both trimers exhibit similar overall B- factors (Fig. 2B), as observed in previously published cryo models of MCRred1-silent (SI Fig. 3A).

3.1.1. Modified amino acids

We have identified the six previously reported modified amino acids in 5AY0 [15], namely, 2-Methyl-glutamine (MGN), S-Methyl-cysteine (SMC), 5-Methyl-arginine (AGM), Di-dehydro-aspartic Acid (DYA), Thioglycine (TG) and N1-Methyl-histidine (MHS) (Fig. 3) in the chain A/a of our new XFEL MCRred1-silent structure as well. Difficulties in purifying active MCR from organisms where a genetic system has been developed have hindered the understanding of the structural or catalytic role(s) of these modified amino acid residues. Thus, we are only able to assign the function of any substituted amino acid based on comparisons of growth rates, which are limited by biosynthesis, not by methanogenesis [42]. Substitution of the thioglycine with a glycine residue in *Methanosarcina acetivorans* did not reveal any growth defects except at elevated temperatures and with substrates that have low free energy yields [43]. It was proposed that the thioglycine residue is not involved directly in catalysis, but in stabilizing the protein secondary structure; however, as just mentioned, the growth rate would not be limited by enzymatic activity of the variant(s), unless it is severely reduced. It is important to complement such studies with activity measurements of the wild-type versus variant proteins. Therefore, we used structural analysis of the *M. marburgensis* enzyme to see if these residues are dynamic in room temperature crystallography. In this study, we find no evidence of dynamics in these six modified amino acids at room temperature. A structural comparison with previously published cryogenic MCRred1-silent models 3M1V and 5A0Y, reveal that the modified amino acids do not exhibit any significant changes in structure or in B-factors across these three models (Table 1, SI Fig. 4). However, out of all the modified amino acids, N1-Methylated Histidine (MHS) shows highest mobility across all three models tested, and among all the reported modified amino acids. However, we require more studies with the active Ni(I) MCR structure to understand the physiological functions of these unique modifications.

3.1.2. Active site

Superimposition of the cryogenic MCRred1-silent structures (3M1V and 5AY0) with our room temperature structure reveals most of the active site architecture to be conserved structurally (Fig. 4, SI Table 2). However, the distance between the oxygen atom of Glutamine 147 and the catalytic Ni in our RT XFEL MCRred1 structure is observed to be 2.27 Å ± 0.05 and 2.28 Å ± 0.04 in protomers 1 and 2, respectively (Fig. 4B). This indicates a 0.07 ± 0.05 Å and 0.03 Å ± 0.04 Å decrease in the Ni/F430-OE1-(Q147) bond in protomer 1 and 2 respectively of the XFEL structure, compared to the cryogenic model 3M1V (SI Table 2). The accuracy of these positional assignments was determined by perturbation of the structure factors (±[F_{obs}-F_{model}]) of the model using the END RAPID method [44] which allows us to assign coordinate errors to individual atoms. We randomly perturbed the structure factors in the target model in 100 trials, followed by re-refinement of each of the perturbed datasets using Phenix. This generated the standard deviations

Table 1
B factors of modified amino acids in RT vs. Cryo MCRred1-silent structures. The B factors for each atom are extracted from the PDB file and added for each specific modified amino acid residue. Here we display average calculated B factors for both MCRred1-silent monomers, separated by commas.

	RT XFEL (Å^2)	CRYO 3M1V (Å^2)	CRYO 5A0Y (Å^2)
2-Methyl Glutamine (MGN400)	22.4, 22.3	7.2, 6.9	8.0, 7.2
5-Methyl Arginine (AGM271)	22.5, 21.7	6.8, 6.5	6.6, 6.6
1-Methylated Histidine (MHS257)	35.1, 32.0	18.0, 15.2	12.8, 11.9
S-Methyl Cysteine (SMC452)	23.7, 24.4	7.8, 8.0	8.5, 8.5
ThioGlycine (TG445)	23.0, 22.9	6.8, 6.5	7.6, 6.7
DI-Dehydro Aspartic Acid (DYA450)	23.4, 22.6	7.9, 8.2	8.4, 8.3

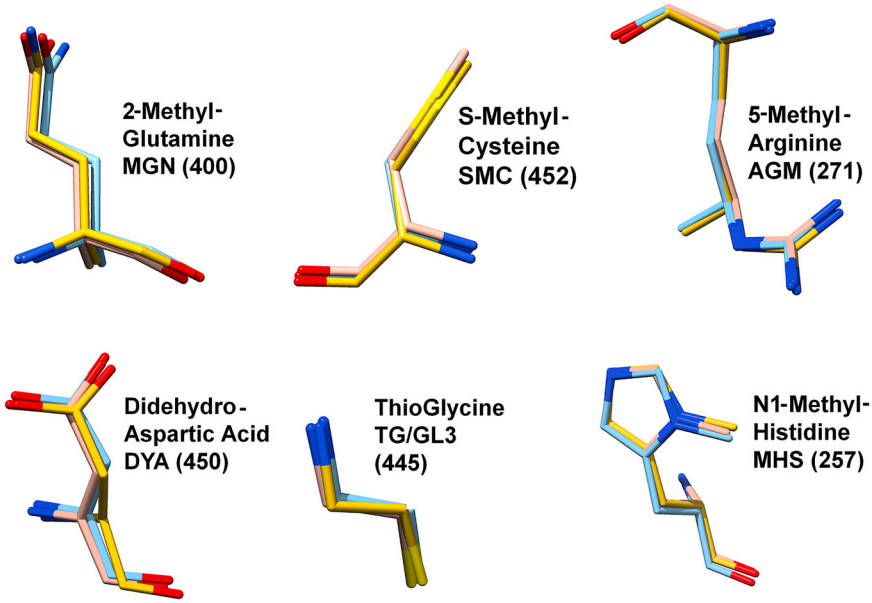

Fig. 3. Modified amino acids in the active site of MCR. In this room temperature structure, these modified residues, namely 2-Methyl-glutamine (MGN), S-Methyl-cysteine (SMC), 5-Methyl-arginine (AGM), Di-dehydro-aspartic Acid (DYA), Thioglycine (TG) and N1-Methyl-histidine (MHS), in MCRred1-silent (yellow) compared with previously collected cryo MCRred1-silent structures (cyan 3M1V, pink 5AY0) show no major structural variations nor fluctuations in B factors across all three structures (Inset & Table 1). B factors normalized according to equation one in a study published by Johnson et al. [51]. Figures made with COOT, Chimera and Chimera-X [32,36,37]. (For interpretation of the references to colour in this figure legend, the reader is referred to the web version of this article.)

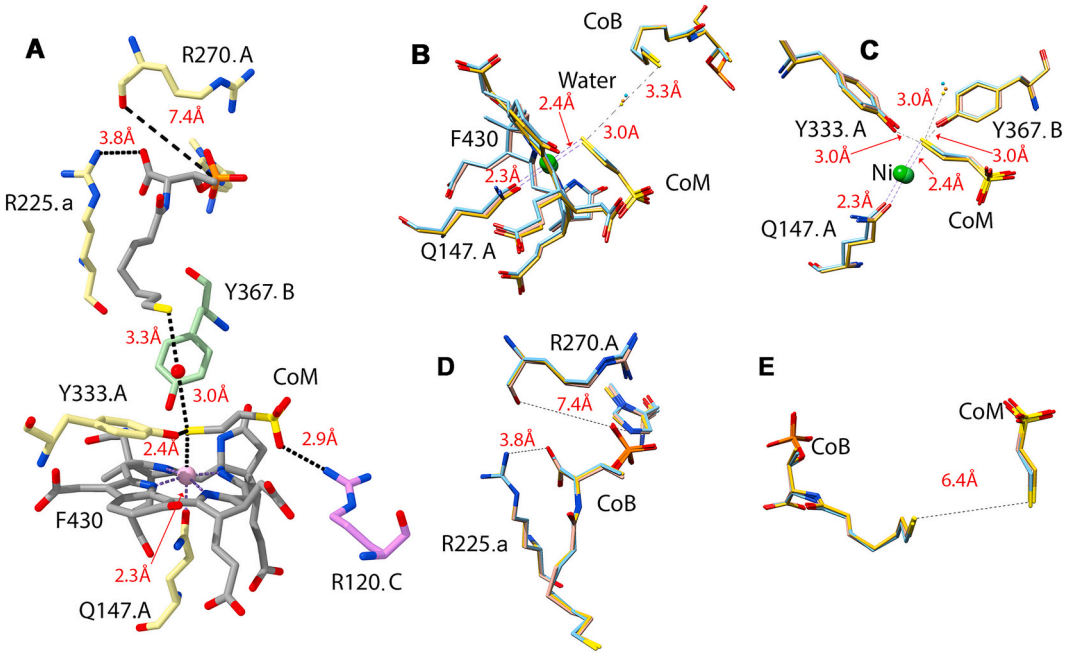

Fig. 4. A: Active site of MCRred1-silent shows conserved water (shown as red sphere) located halfway between CoM and CoB substrates. (B-E): Different views of key active site residues in previously collected cryo MCRred1-silent structures (cyan 3M1V, salmon 5AY0) superimposed on our RT structure (yellow) show that these structures have similar active site organization. (For interpretation of the references to colour in this figure legend, the reader is referred to the web version of this article.)

of the reported positions. Although this distance shrinking in the RT MCR model is exciting, it must be noted that at his current data resolution this observation is within the error limits and hence it is not possible to draw further conclusions from this observation

Another distinction between the structures is a 0.24 Å ± 0.09 expansion in the distance between the two thiolates of CoM and CoB in protomer 1 (negligible change in protomer 2) with respect to the cryogenic model 3M1V.

3.1.3. Substrate analog CoM (Coenzyme M) & native substrate HSCoB

We see the substrate analog CoM (100% occupancy) as well as the native substrate HSCoB (~ 90% occupancy) bound to the active site of our room temperature XFEL MCRred1-silent structure, with visible 2Fo-fc electron density at 1.5 sigma (SI Fig. 5B). CoM and HSCoB thiolates are at about 2.4 Å and 8.8 Å distances respectively from the catalytic Ni (SI Table 3). Retention of CoM and CoB is a little surprising, given that the purified protein had been subjected to seven rounds of buffer exchange; however, CoM and HSCoB are also found in the cryogenic structures of this form of MCR [15,17]. The thiol of HSCoB is only coordinated by a nearby (~2.6 Å away) N481 (chain A/a) and a water (~3 Å away); however, CoB interacts strongly with several nearby residues via its threonine phosphate end (SI Fig. 6). This CoB-phosphate coordination is also intact in the cryogenic MCRred1-silent structures (3M1V and 5A0Y), which makes the retention of CoB following oxidation and several rounds of buffer exchange in our study, quite logical. The retention of CoM within the crystal active site can be potentially explained owing to its coordination via its thiolate group to the Ni atom and three other active site residues, namely Y333-OH, Y367-OH, Ni, and a water (SI fig. 7)

These observations point to a potential mechanistic feature of MCR wherein it assumes a "locked-in" state as soon as the catalytic Ni is oxidized. This hypothesis is further bolstered by the overall similarities observed in the active site architecture of the RT XFEL structure compared to previously published cryogenic structures of MCRred1, although this requires further exploration. Furthermore, CoM is positioned as in the cryo structures, with the sulfur of CoM located near the Ni center (SI Fig. 7). It should be noted that CH_3-CoM is not present in our structure, as it was not present in our crystallization solution. However, previous attempts in the field to crystallize MCR with CH_3-SCoM have yielded several synchrotron cryo structures that lack the methyl group of CH_3-SCoM [17]. Grabarse et al. suggest radiation damage-induced conversion of the CH_3-SCoM to CoM at synchrotron sources [16]. This observation highlights the need to use XFEL to record damage-free structures of MCR co-crystallized with CH_3-SCoM and track its fate within the active site.

Interestingly, we notice significant 2Fo-Fc electron density roughly halfway between the thiol groups of CoM and CoB (SI Fig. 5), at about 1.7 sigma in protomer 1 and 1.4 sigma in protomer 2. This "mystery" 2Fo-Fc electron density has also been reported previously in cryogenic structures of both MCR and ECR, wherein a water molecule was fit in to explain the density in MCR. However, there is debate about the identity of this molecule. While some favor water, others suggest the density might be explained best by a molecule having one or two heavier atoms in MCR and ECR, respectively [45]. We placed a water molecule between the two substrate thiol groups in both protomers of MCRred1-silent (Fig. 4C). This water has an average B factor of ~32 $Å^2$ in our room-temperature structure. Furthermore, there is no significant B factor elevation within a radius of ~20 Å centered on this active site water in both protomers in our room-temperature structure or in the cryo structures of 3M1V or 5A0Y [15,17]. These factors support the assignment of this density to a "conserved" and well-ordered water molecule that remains coordinated to the active site of MCRred1-silent (SI Fig. 5). While this water molecule appears to be well conserved in the Ni(II) state of the MCR enzyme, it is unlikely to be present during catalysis [14]. We suggest that the water molecule in this "locked-in" Ni(II) MCR structure acts as a placeholder for the methyl radical during the transition state.

There is one major difference between the coordination environment of the assigned water molecule in our structure versus those of the cryogenic structures (SI Fig. 6). In protomer 1 of the RT structure, the water molecule is not coordinated to the CoB thiol but instead only weakly coordinated to the thiolate of CoM (3.05 Å away) unlike in the

cryogenic structures (3M1V and 5A0Y) where it associates with the CoB thiol, 2.8 Å and 2.96 Å away, respectively. The distance between the water and the CoM thiolate in the cryogenic models 3M1V and 5A0Y are expanded to 3.5 Å and 3.3 Å compared to the 3.05 Å in the RT structure. This distance elongation in the cryogenic structures could potentially indicate evidence of radiation damage or partial motion of the water molecule at room temperature. However, in protomer 2 of the RT structure, this water-CoB sulfur thiolate coordination is intact (distance between the water and sulfur of CoB is 2.99 Å), like in the cryogenic models. Moreover, this water molecule is close to two active site tyrosines nearby, namely Y333 and Y367 (~3.0 Å away from both hydroxyl groups of the tyrosines), which might coordinate it by weakly by donating H bonds via their OH groups (SI Fig. 5A) during catalysis. It will be interesting to further explore the active site water coordination environment as shown in SI Fig. 5, and its dependence on data collection temperatures to see whether this has a significant impact on the enzyme's catalysis.

3.2. Simultaneous collection of Ni XES for the MCRred1-silent form

We collected Ni Kα X-ray Emission Spectroscopy (XES) simultaneously with XRD data (Fig. 5). These data provide a real-time handle to monitor both oxidation state and electronic structure during Serial Femtosecond Crystallography [46,47]. The oxidized MCR data was compared against those of two water-soluble nickel(II) standards, $[Ni(H2O)6]^{2+}$ and $[Ni(bpy)3]^{2+}$ (bpy = 2,2′-bipyridine), which were also collected in solution at room temperature at the XFEL using the DOT sample delivery system. The XES spectrum of the Ni center in the oxidized MCR is significantly shifted from both molecular standards.

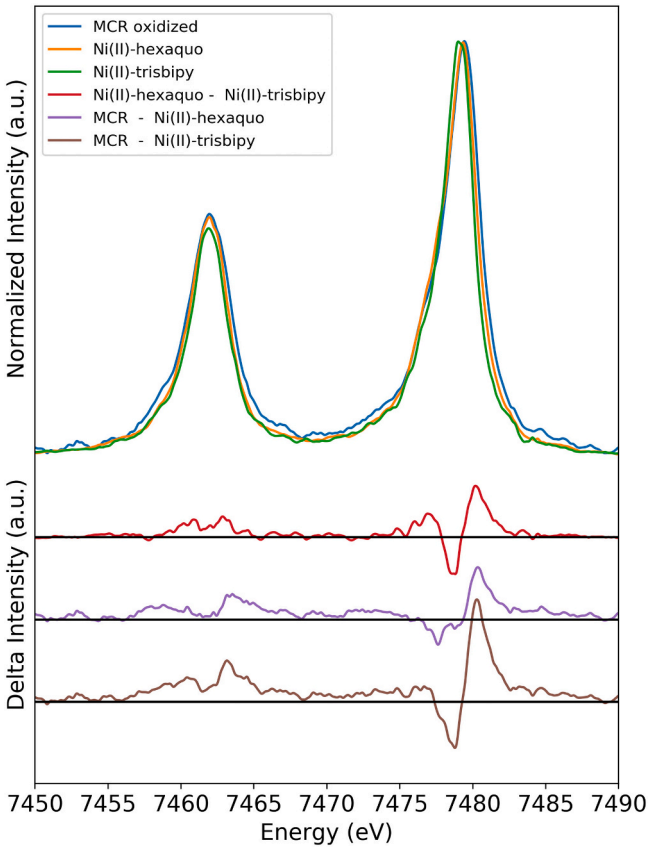

Fig. 5. Ni Kα XES spectrum of the MCRred1-silent crystals collected simultaneously with the XRD data at the XFEL. Spectra of solutions of two molecular standards, [Ni hexaquo, $Ni(H2O)6]^{2+}$ and [Ni(II)-trisbipy, $Ni(bpy)3]^{2+}$ collected at the XFEL are also shown. Difference spectra between the MCR and the molecular standards are presented.

That such a clear difference is observed between complexes in similar oxidation state, but with changes only in the coordination environment implies that XES will be a useful tool to monitor subtle changes to the electronic structure of the Ni center in MCR during future experiments in which we will collect simultaneous XRD and XES snapshots of the catalytic cycle by SFX.

3.3. Identification of potential "gas tunnel" residues in MCR-Ni(II)

Recently, the crystal structure of an MCR homolog, ECR, isolated from the ethane oxidizing organism *Candadatus* Ethanoperedens thermophilum, was reported by Hahn et al. via xenon pressurized cryo-crystallography [45], wherein a 33 Å long gas tunnel was discovered, leading from the substrate binding cavity to the surface [45], as shown in Fig. 6. When the same technique was performed on the MCR purified from the methane producing *M. marburgensis*, six Xe atoms were found in each protomer, all at the surface of the enzyme, leading Hahn et al. to suggest that the gas tunnel is specific to ethane oxidizers [45]. Our independent xenon pressurized cryo-crystallographic structure of the *M. marburgensis* MCR revealed four xenon binding sites (Fig. 6). Of these four sites, Xe1 and Xe2 are found near the surface of the B subunit, Xe3 at the surface of the A subunit, and Xe4 in the B subunit 22 Å from the catalytic Ni (Fig. 6, SI Fig. 8). To validate Hahn et al's observation of no methane transport tunnel present in MCR, we superimposed our Xe-pressurized MCR structure with ECR (PDB 7B1S). We noticed that Xe3 is ~11 Å away from the ECR gas tunnel (Fig. 6), but found no indication of a "tunnel" in MCR by computational analysis using Caver [40] or by Xe pressurized crystallography, as previously shown by Hahn et al, who proposed that this tunnel exists specifically for ethane oxidizers [45].

To perform a more extensive investigation into the difference between methane and ethane oxidizers, we performed sequence alignment of MCR from *M. marburgensis* with ECR (PDB 7B1S) via Clustal-W [41] and identified several common residues in both enzymes that line the putative ECR gas tunnel (SI Fig. 9). Out of these residues, three hydrophilic residues of *M. marburgensis* (namely K351, E355, and E487 in chain A of 3M1V) align to Ca. *E. thermophilum* hydrophobic residues (namely A392, M398, and G532 respectively; 7B1S numbering), highlighted in red in SI Fig. 9. The first two of these residues in ECR are located at the opening of this ethane gas tunnel, while the latter is located in the middle of the tunnel. A comparison of these residues in the ECR 7B1S structure with the MCR cryogenic 3M1V structure yields no significant differences in structure or B factors. Moreover, in all the models (cryo ECR, cryo MCR and RT MCR), the side chains of K351 and E355 have the highest B factors compared to their surrounding residues (within ~15 Å). It will be interesting to use the room temperature DOT and XFEL methods to further investigate the possibility of a gas tunnel in MCR by tracking structural differences and B factor changes in these conserved tunnel residues after adding substrates (and analogs/inhibitors like CoM) to MCR.

4. Discussion

While previous crystallography studies have provided the foundation for understanding the mechanism of MCR catalysis [14–18], capturing the structure of the enzyme in the active Ni(I) state is still a goal to be achieved. Therefore, the elucidation of MCR's active structure and visualization of conformational dynamics along the reaction cycle will depend on the evolution of techniques in structural biology. In this study commemorating Dick Holm and his contribution to the field of Ni complexes, we demonstrate the feasibility of using our DOT sample delivery approach to perform simultaneous XRD and XES data collection on the Ni- dependent MCR protein system. This approach will be critical in characterizing the structural, as well as electronic state progression of the catalytic Ni as MCR undergoes catalysis. Herein, we present the first room temperature structure of MCRred1-silent Ni(II) state using the X-ray Free-Electron Laser (XFEL) source at LCLS, SLAC.

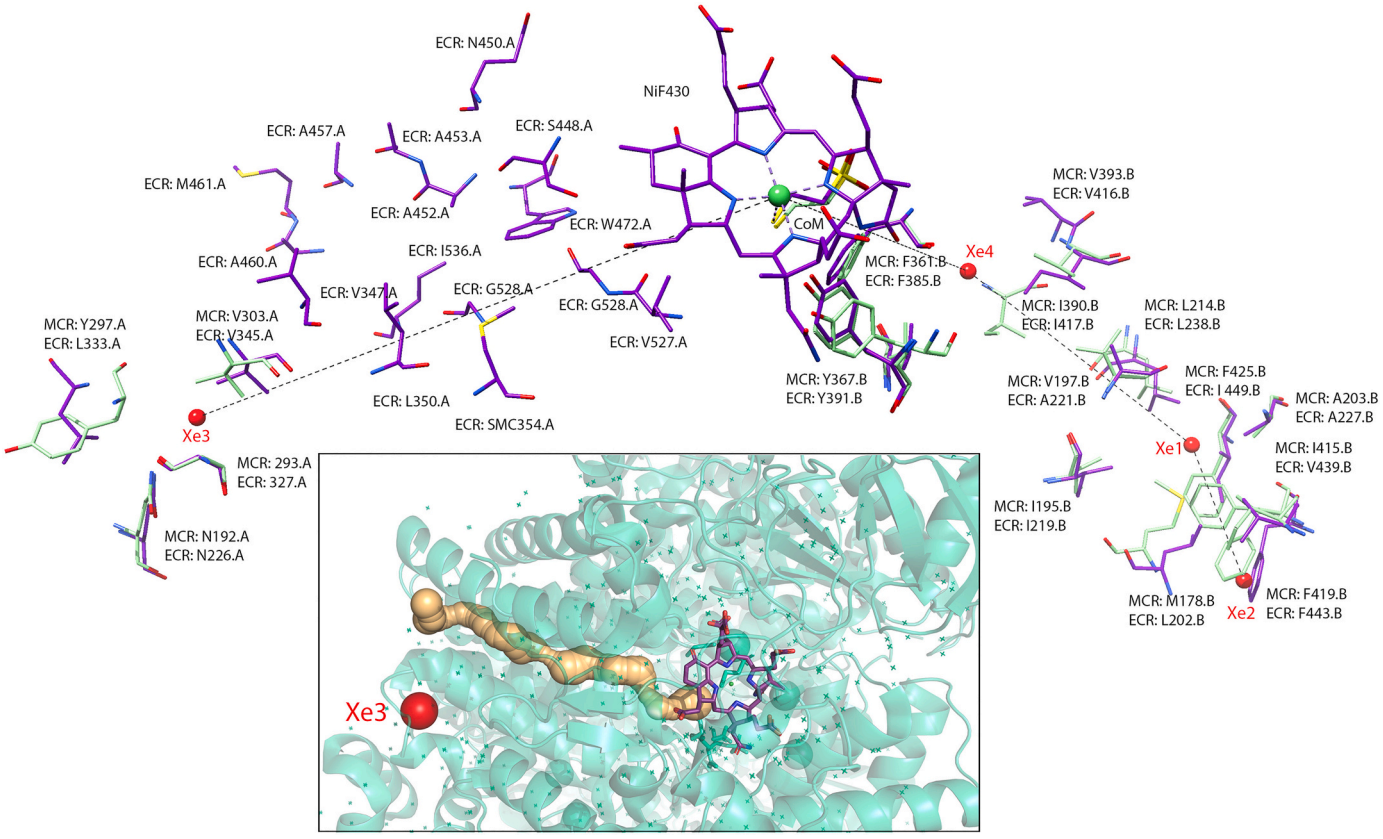

Fig. 6. Using xenon to map gas channels in MCR and ECR. (A) An overall view of the four Xe locations in MCR. Xe 3 is located close to (~11 Å away from) the putative ECR gas tunnel. (Inset) Caver analysis of ECR to visualize the gas tunnel in relation to Xe3 in the MCR pressurized cryo structure (B) Location of Xe1, 2 and 4 and the surrounding residues in the MCR Xe pressurized cryo structure (green) superimposed with the corresponding ECR (PDB ID 7B1S) residues (purple). Inset: Location of MCR Xe 3 and superimposed key surrounding residues in MCR (green) and ECR (purple). (For interpretation of the references to colour in this figure legend, the reader is referred to the web version of this article.)

Comparison of the room temperature and cryogenic MCR structures reveals mostly similarities, but some differences are of note. While we observed an apparent ~0.07 Å shortening of the bond between the lower axial glutamine (Q147) and the Ni(II) in protomer 2 of our RT structure relative to the cryogenic MCR structure (3M1V) (0.03 Å bond shortening in protomer 1), high resolution data is needed to confirm if this is significant. A second distinction pertains to the loss of coordination of the water molecule in our RT structure with the thiol of CoB in protomer 1 (this coordination is retained in both cryogenic structures 3M1V and 5A0Y in protomer 1). Third, we notice that the distance between the thiolate of CoM and the thiol of CoB expands by an average of ~0.24 Å in one of the protomers in the RT structure compared to the cryogenic structure, 3M1V, with no changes in these distances in the other protomer. These last two variations observed in the room-temperature structure represent small changes in the locations of CoM and CoB relative to those seen in previous cryo structures. While these subtle differences are interesting and warrant additional investigations, we require higher quality datasets at RT to better resolve them, which is our continuing goal.

We had hoped that our room temperature structure might reveal evidence supporting a proposal, based on electron paramagnetic resonance and UV–visible spectroscopic studies of the active Ni(I) enzyme, that MCR exhibits half-of-sites reactivity. This hypothesis envisions that the two MCR active sites are structurally connected such that one active site can undergo catalysis, like the motion of a "dual stroke motor" [45]. However, in our room-temperature Ni(II) structure, we observe similar B-factors between the related protomers, even near the active site. Therefore, if this model is correct, it appears that the dynamical differences may be observed only in the structure of the Ni(I) form of MCR, further underlining the need for capturing the structure of the active state of this enzyme, especially at room temperature. Furthermore, these overall structural similarities between the RT and cryogenic structures, as well as the retention of CoBSH in the active site of our RT MCRred1-silent structure point to a potential "locked-in" state of the Ni(II) MCR enzyme's catalytic cavity.

Due to the lack of movement in the "locked-in" state of Ni(II) MCR, to observe any important conformational dynamics relevant to its catalysis, we require a complete structural characterization of the active Ni(I) MCR form as it turns over at physiologically relevant temperatures. While previous solution XAS studies of MCRred1 have revealed the local coordination environment of the Ni center in various states [19], the overall crystal structure of MCR and its catalytic intermediates is a challenge that we hope can be met by future XFEL studies. This active MCR structure will provide a clear visual representation of the active site, substrate binding modes, and methane localization as it lights the fuse for methane production and oxidation.

Obtaining the structure of the Ni(I) form of MCR is challenging because the most reliable methods of activation are by sparging cell cultures with H_2 [48] or, as used in this study, CO [49]. Moreover, oxidative damage irreversibly converts the active enzyme to a Ni(II) form. We are currently working on resolving some of these obstacles by batch co-crystallizing MCR with reducing agents and developing protocols for anaerobic data collection. We will screen these co-microcrystals for shifts in unit cell parameters from MCR Ni(II), potentially indicating a change in oxidation state. We hope to take advantage of MCR's strictly ordered catalytic mechanism [13] to synchronize the turnover process in all the microcrystals. To maintain this synchronicity in each crystal, we will co-crystallize the Ni(I) enzyme with the native

substrate, CH_3-SCoM, and use the Drop-On-Drop-On-Tape sample delivery system to deliver CoBSH in order to trigger catalysis [50].

In conclusion, this current study serves as a good starting point that demonstrates i) the feasibility of using our Drop-On-Tape (DOT) sample delivery technique to capture the electronic state of the catalytic Ni atom via XES, while simultaneously collecting a complete 1.9 Å XRD dataset in less than one hour. ii) While we do not see large structural differences between our XFEL and published cryogenic MCRred1-silent structures, we do see indications that the active site "locks" in place following Ni(I) oxidation, thereby retaining the CoM analog and native CoB substrates. In the future, we want to build on this demonstrated simultaneous XRD and XES technique to trigger and track damage free catalysis in active Ni(I)-MCR *in crystallo* using anaerobic sample delivery and data collection at XFEL sources.

Author contributions

Conceptualization; J.Y., J.F.K., S.W.R. Sample Purification and Crystallization: C.J.O., A.P. XFEL setup design for XES and XRD: R.A.-M., F.D.F., H.M., P.S.S. Data collection at LCLS: M.D., S.M.K., C.K., I.B., H. M., P.S.S., L.B.G., R. A.-M., F.M., F.D.F., Al.B., U.B., V.K.Y., J.Y., J.F.K. SR Data collection: M.D. R.C., P.Y.-T.C., C.L.D., XRD Data Analysis: M. D., P.Y.-T.C., C.L.D., A.B, A.S.B., D.W.P., N.K.S. XES Data Analysis. C.K., I.B., H.M., M.D.D., R.M., T.F., U.B. Structure Refinement: C.J.O., M.D., P.Y.-T.C., S.M.K., N.W.M. C.L.D. Writing – Original Draft: M.D., C.J.O., S.W.R. Writing –Review and Editing, all authors. Supervision: C.L.D., V. K.Y., J.Y., J.F.K, S.W.R.

Declaration of Competing Interest

The authors have no competing interests to declare.

Acknowledgements

We thank staff from LCLS and ALS (BL 5.0.2, 8.2.1 and 8.3.1) for their support. P.Y.-, T.C. and C.L.D. thank Dr. Corie Ralston and Dr. Steven E. Cohen for helping with Xe-pressurized cryo- crystallography. C.L.D. is a Howard Hughes Medical Institute investigator and a Fellow of the Bio- inspired Solar Energy Program, Canadian Institute for Advanced Research. This work was supported by the Director, Office of Science, Office of Basic Energy Sciences (OBES), Division of Chemical Sciences, Geosciences, and Biosciences of the Department of Energy (DOE) (J.Y., V.K.Y., J.F.K.) for X-ray methodology and instrumentation and spectroscopy and crystallography data collection and analysis, by National Institutes of Health, National Institute of General Medical Sciences (NIH NIGMS) grants 1P41GM139687 (R.A.-M.), GM55302 (V.K.Y.), GM110501 (J.Y.), GM126289 (J.F.K.), GM117126 (N.K.S.), R35 GM126982 (C.L.D.), PO1GM063210 (N.W.M). Vetenskapsrådet 2017-00356 (T.F.), and the Air Force Office of Scientific Research grant FA8655-20-1-7010 (T.F.) are acknowledged for support. This work also was supported by the Physical Biosciences Program within the OBES at DOE by contract DE-FG02-08ER15931 (S.W.R.). Beamlines 5.0.2, 8.2.1, 8.2.2 and 8.3.1 of the Advanced Light Source, a DOE Office of Science User Facility under Contract No. DE-AC02-05CH11231, are supported in part by the ALS-ENABLE Program funded by the NIH NIGMS, grant P30 GM124169-01. Use of the LCLS, SLAC National Accelerator Laboratory, is supported by the US DOE, Office of Science, OBES under contract DE-AC02-76SF00515. The Rayonix detector used at LCLS was supported by the NIH NIGMS grant S10 OD023453. This research used resources of the National Energy Research Scientific Computing Center, a User Facility supported by the Office of Science, DOE, under contract DE-AC02-05CH11231.

Appendix A. Supplementary data

Supplementary data to this article can be found online at https://doi.org/10.1016/j.jinorgbio.2022.111768.

References

[1] G. Yvon-Durocher, A.P. Allen, D. Bastviken, R. Conrad, C. Gudasz, A. St-Pierre, N. Thanh-Duc, P.A. del Giorgio, Methane fluxes show consistent temperature dependence across microbial to ecosystem scales, Nature 507 (2014) 488–491, https://doi.org/10.1038/nature13164.

[2] R.K. Thauer, Biochemistry of methanogenesis: a tribute to Marjory Stephenson. 1998 Marjory Stephenson Prize Lecture, Microbiology (Reading) 144 (Pt 9) (1998) 2377–2406, https://doi.org/10.1099/00221287-144-9-2377.

[3] O. Badr, S.D. Probert, P.W. O'Callaghan, Sinks for atmospheric methane, Appl. Energy 41 (1992) 137–147, https://doi.org/10.1016/0306-2619(92)90041-9.

[4] S. Kirschke, P. Bousquet, P. Ciais, M. Saunois, J.G. Canadell, E.J. Dlugokencky, P. Bergamaschi, D. Bergmann, D.R. Blake, L. Bruhwiler, P. Cameron-Smith, S. Castaldi, F. Chevallier, L. Feng, A. Fraser, M. Heimann, E.L. Hodson, S. Houweling, B. Josse, P.J. Fraser, P.B. Krummel, J.-F. Lamarque, R. L. Langenfelds, C. Le Quéré, V. Naik, S. O'Doherty, P.I. Palmer, I. Pison, D. Plummer, B. Poulter, R.G. Prinn, M. Rigby, B. Ringeval, M. Santini, M. Schmidt, D.T. Shindell, I.J. Simpson, R. Spahni, L.P. Steele, S.A. Strode, K. Sudo, S. Szopa, G. R. van der Werf, A. Voulgarakis, M. van Weele, R.F. Weiss, J.E. Williams, G. Zeng, Three decades of global methane sources and sinks, Nat. Geosci. 6 (2013) 813–823, https://doi.org/10.1038/ngeo1955.

[5] D.A. Lashof, D.R. Ahuja, Relative contributions of greenhouse gas emissions to global warming, Nature 344 (1990) 529–531, https://doi.org/10.1038/344529a0.

[6] C.K. Singh, A. Kumar, S.S. Roy, Quantitative analysis of the methane gas emissions from municipal solid waste in India, Sci. Rep. 8 (2018) 2913, https://doi.org/10.1038/s41598-018-21326-9.

[7] J. Tollefson, IPCC climate report: earth is warmer than it's been in 125,000 years, Nature 596 (2021) 171–172, https://doi.org/10.1038/d41586-021-02179-1.

[8] D. Ankel-Fuchs, R.K. Thauer, Methane formation from methyl-coenzyme M in a system containing methyl-coenzyme M reductase, component B and reduced cobalamin, Eur. J. Biochem. 156 (1986) 171–177, https://doi.org/10.1111/j.1432-1033.1986.tb09563.x.

[9] S. Shima, M. Krueger, T. Weinert, U. Demmer, J. Kahnt, R.K. Thauer, U. Ermler, Structure of a methyl-coenzyme M reductase from Black Sea mats that oxidize methane anaerobically, Nature 481 (2012) 98–101, https://doi.org/10.1038/nature10663.

[10] C. Heller, M. Hoppert, J. Reitner, Immunological localization of coenzyme M reductase in anaerobic methane-oxidizing Archaea of ANME 1 and ANME 2 type, Geomicrobiol J. 25 (2008) 149–156, https://doi.org/10.1080/01490450802006884.

[11] T. Wongnate, S.W. Ragsdale, The reaction mechanism of methyl-coenzyme M reductase, J. Biol. Chem. 290 (2015) 9322–9334, https://doi.org/10.1074/jbc.M115.636761.

[12] S. Chen, V. Pelmenschikov, M.R.A. Blomberg, P.E.M. Siegbahn, Is there a Ni-methyl intermediate in the mechanism of methyl-coenzyme M reductase? J. Am. Chem. Soc. 131 (2009) 9912–9913, https://doi.org/10.1021/ja904301f.

[13] T. Wongnate, D. Sliwa, B. Ginovska, D. Smith, M.W. Wolf, N. Lehnert, S. Raugei, S. W. Ragsdale, The radical mechanism of biological methane synthesis by methyl-coenzyme M reductase, Science 352 (2016) 953–958, https://doi.org/10.1126/science.aaf0616.

[14] U. Ermler, W. Grabarse, S. Shima, M. Goubeaud, R.K. Thauer, Crystal structure of methyl-coenzyme M reductase: the Key enzyme of biological methane formation, Science 278 (1997) 1457–1462, https://doi.org/10.1126/science.278.5342.1457.

[15] T. Wagner, J. Kahnt, U. Ermler, S. Shima, Didehydroaspartate modification in methyl-coenzyme M reductase catalyzing methane formation, Angew. Chem. Int. Ed. 55 (2016) 10630–10633, https://doi.org/10.1002/anie.201603882.

[16] W. Grabarse, F. Mahlert, E.C. Duin, M. Goubeaud, S. Shima, R.K. Thauer, V. Lamzin, U. Ermler, On the mechanism of biological methane formation: structural evidence for conformational changes in methyl-coenzyme M reductase upon substrate binding, J. Mol. Biol. 309 (2001) 315–330, https://doi.org/10.1006/jmbi.2001.4647.

[17] P.E. Cedervall, M. Dey, A.R. Pearson, S.W. Ragsdale, C.M. Wilmot, Structural insight into methyl-coenzyme M reductase chemistry using coenzyme B analogues, Biochemistry 49 (2010) 7683–7693, https://doi.org/10.1021/bi100458d.

[18] P.E. Cedervall, M. Dey, X. Li, R. Sarangi, B. Hedman, S.W. Ragsdale, C.M. Wilmot, Structural analysis of a Ni-methyl species in methyl-coenzyme M reductase from *Methanothermobacter marburgensis*, J. Am. Chem. Soc. 133 (2011) 5626–5628, https://doi.org/10.1021/ja110492p.

[19] A. Patwardhan, R. Sarangi, B. Ginovska, S. Raugei, S.W. Ragsdale, Nickel-sulfonate mode of substrate binding for forward and reverse reactions of methyl-SCoM reductase suggest a radical mechanism involving long-range electron transfer, J. Am. Chem. Soc. 143 (2021) 5481–5496, https://doi.org/10.1021/jacs.1c01086.

[20] T. Weinert, N. Olieric, R. Cheng, S. Brünle, D. James, D. Ozerov, D. Gashi, L. Vera, M. Marsh, K. Jaeger, F. Dworkowski, E. Panepucci, S. Basu, P. Skopintsev, A. S. Doré, T. Geng, R.M. Cooke, M. Liang, A.E. Prota, V. Panneels, P. Nogly, U. Ermler, G. Schertler, M. Hennig, M.O. Steinmetz, M. Wang, J. Standfuss, Serial millisecond crystallography for routine room-temperature structure determination at synchrotrons, Nat. Commun. 8 (2017) 542, https://doi.org/10.1038/s41467-017-00630-4.

[21] E. Nango, A. Royant, M. Kubo, T. Nakane, C. Wickstrand, T. Kimura, T. Tanaka, K. Tono, C. Song, R. Tanaka, T. Arima, A. Yamashita, J. Kobayashi, T. Hosaka, E. Mizohata, P. Nogly, M. Sugahara, D. Nam, T. Nomura, T. Shimamura, D. Im, T. Fujiwara, Y. Yamanaka, B. Jeon, T. Nishizawa, K. Oda, M. Fukuda, R. Andersson,

P. Båth, R. Dods, J. Davidsson, S. Matsuoka, S. Kawatake, M. Murata, O. Nureki, S. Owada, T. Kameshima, T. Hatsui, Y. Joti, G. Schertler, M. Yabashi, A.-N. Bondar, J. Standfuss, R. Neutze, S. Iwata, A three-dimensional movie of structural changes in bacteriorhodopsin, Science 354 (2016) 1552–1557, https://doi.org/10.1126/science.aah3497.

[22] R.C. Kunz, Y.-C. Horng, S.W. Ragsdale, Spectroscopic and kinetic studies of the reaction of bromopropanesulfonate with methyl-coenzyme M reductase*, J. Biol. Chem. 281 (2006) 34663–34676, https://doi.org/10.1074/jbc.M606715200.

[23] R.G. Sierra, A. Batyuk, Z. Sun, A. Aquila, M.S. Hunter, T.J. Lane, M. Liang, C. H. Yoon, R. Alonso-Mori, R. Armenta, J.-C. Castagna, M. Hollenbeck, T.O. Osier, M. Hayes, J. Aldrich, R. Curtis, J.E. Koglin, T. Rendahl, E. Rodriguez, S. Carbajo, S. Guillet, R. Paul, P. Hart, K. Nakahara, G. Carini, H. DeMirci, E.H. Dao, B. M. Hayes, Y.P. Rao, M. Chollet, Y. Feng, F.D. Fuller, C. Kupitz, T. Sato, M. H. Seaberg, S. Song, T.B. van Driel, H. Yavas, D. Zhu, A.E. Cohen, S. Wakatsuki, S. Boutet, The macromolecular femtosecond crystallography instrument at the linac coherent light source, J. Synchrotron. Rad. 26 (2019) 346–357, https://doi.org/10.1107/S1600577519001577.

[24] F.D. Fuller, S. Gul, R. Chatterjee, E.S. Burgie, I.D. Young, H. Lebrette, V. Srinivas, A.S. Brewster, T. Michels-Clark, J.A. Clinger, B. Andi, M. Ibrahim, E. Pastor, C. de Lichtenberg, R. Hussein, C.J. Pollock, M. Zhang, C.A. Stan, T. Kroll, T. Fransson, C. Weninger, M. Kubin, P. Aller, L. Lassalle, P. Bräuer, M.D. Miller, M. Amin, S. Koroidov, C.G. Roessler, M. Allaire, R.G. Sierra, P.T. Docker, J.M. Glownia, S. Nelson, J.E. Koglin, D. Zhu, M. Chollet, S. Song, H. Lemke, M. Liang, D. Sokaras, R. Alonso-Mori, A. Zouni, J. Messinger, U. Bergmann, A.K. Boal, J.M. Bollinger, C. Krebs, M. Högbom, G.N. Phillips, R.D. Vierstra, N.K. Sauter, A.M. Orville, J. Kern, V.K. Yachandra, J. Yano, Drop-on-demand sample delivery for studying biocatalysts in action at X-ray free-electron lasers, Nat. Methods 14 (2017) 443–449, https://doi.org/10.1038/nmeth.4195.

[25] R. Alonso-Mori, J. Kern, D. Sokaras, T.-C. Weng, D. Nordlund, R. Tran, P. Montanez, J. Delor, V.K. Yachandra, J. Yano, U. Bergmann, A multi-crystal wavelength dispersive x-ray spectrometer, Rev. Sci. Instrum. 83 (2012), 073114, https://doi.org/10.1063/1.4737630.

[26] G. Winter, D.G. Waterman, J.M. Parkhurst, A.S. Brewster, R.J. Gildea, M. Gerstel, L. Fuentes-Montero, M. Vollmar, T. Michels-Clark, I.D. Young, N.K. Sauter, G. Evans, DIALS: implementation and evaluation of a new integration package, Acta Cryst. D 74 (2018) 85–97, https://doi.org/10.1107/S2059798317017235.

[27] A.S. Brewster, D.G. Waterman, J.M. Parkhurst, R.J. Gildea, I.D. Young, L. J. O'Riordan, J. Yano, G. Winter, G. Evans, N.K. Sauter, Improving signal strength in serial crystallography with DIALS geometry refinement, Acta Cryst. D 74 (2018) 877–894, https://doi.org/10.1107/S2059798318009191.

[28] J. Hattne, N. Echols, R. Tran, J. Kern, R.J. Gildea, A.S. Brewster, R. Alonso-Mori, C. Glöckner, J. Hellmich, H. Laksmono, R.G. Sierra, B. Lassalle-Kaiser, A. Lampe, G. Han, S. Gul, D. DiFiore, D. Milathianaki, A.R. Fry, A. Miahnahri, W.E. White, D. W. Schafer, M.M. Seibert, J.E. Koglin, D. Sokaras, T.-C. Weng, J. Sellberg, M. J. Latimer, P. Glatzel, P.H. Zwart, R.W. Grosse-Kunstleve, M.J. Bogan, M. Messerschmidt, G.J. Williams, S. Boutet, J. Messinger, A. Zouni, J. Yano, U. Bergmann, V.K. Yachandra, P.D. Adams, N.K. Sauter, Accurate macromolecular structures using minimal measurements from X-ray free-electron lasers, Nat. Methods 11 (2014) 545–548, https://doi.org/10.1038/nmeth.2887.

[29] P.R. Evans, An introduction to data reduction: space-group determination, scaling and intensity statistics, Acta Crystallogr. D Biol. Crystallogr. 67 (2011) 282–292, https://doi.org/10.1107/S090744491003982X.

[30] D. Liebschner, P.V. Afonine, M.L. Baker, G. Bunkóczi, V.B. Chen, T.I. Croll, B. Hintze, L.W. Hung, S. Jain, A.J. McCoy, N.W. Moriarty, R.D. Oeffner, B.K. Poon, M.G. Prisant, R.J. Read, J.S. Richardson, D.C. Richardson, M.D. Sammito, O. V. Sobolev, D.H. Stockwell, T.C. Terwilliger, A.G. Urzhumtsev, L.L. Videau, C. J. Williams, P.D. Adams, Macromolecular structure determination using X-rays, neutrons and electrons: recent developments in Phenix, Acta Crystallogr. D Struct. Biol. 75 (2019) 861–877, https://doi.org/10.1107/S2059798319011471.

[31] A.J. McCoy, R.W. Grosse-Kunstleve, P.D. Adams, M.D. Winn, L.C. Storoni, R. J. Read, Phaser crystallographic software, J. Appl. Crystallogr. 40 (2007) 658–674, https://doi.org/10.1107/S0021889807021206.

[32] P. Emsley, B. Lohkamp, W.G. Scott, K. Cowtan, Features and development of Coot, Acta Cryst. D 66 (2010) 486–501, https://doi.org/10.1107/S0907444910007493.

[33] P.D. Adams, P.V. Afonine, G. Bunkóczi, V.B. Chen, I.W. Davis, N. Echols, J. J. Headd, L.-W. Hung, G.J. Kapral, R.W. Grosse-Kunstleve, A.J. McCoy, N. W. Moriarty, R. Oeffner, R.J. Read, D.C. Richardson, J.S. Richardson, T. C. Terwilliger, P.H. Zwart, PHENIX: a comprehensive Python-based system for macromolecular structure solution, Acta Crystallogr. D Biol. Crystallogr. 66 (2010) 213–221, https://doi.org/10.1107/S0907444909052925.

[34] P.V. Afonine, R.W. Grosse-Kunstleve, N. Echols, J.J. Headd, N.W. Moriarty, M. Mustyakimov, T.C. Terwilliger, A. Urzhumtsev, P.H. Zwart, P.D. Adams, Towards automated crystallographic structure refinement with phenix.refine, Acta Cryst. D 68 (2012) 352–367, https://doi.org/10.1107/S0907444912001308.

[35] P. Emsley, K. Cowtan, Coot: model-building tools for molecular graphics, Acta Crystallogr. D60 (2004) 2126–2132 (n.d).

[36] E.F. Pettersen, T.D. Goddard, C.C. Huang, G.S. Couch, D.M. Greenblatt, E.C. Meng, T.E. Ferrin, UCSF Chimera—a visualization system for exploratory research and analysis, J. Comput. Chem. 25 (2004) 1605–1612, https://doi.org/10.1002/jcc.20084.

[37] E.F. Pettersen, T.D. Goddard, C.C. Huang, E.C. Meng, G.S. Couch, T.I. Croll, J. H. Morris, T.E. Ferrin, U.C.S.F. ChimeraX, Structure visualization for researchers, educators, and developers, Protein Sci. 30 (2021) 70–82, https://doi.org/10.1002/pro.3943.

[38] Z. Otwinowski, W. Minor, [20] processing of X-ray diffraction data collected in oscillation mode, Methods Enzymol. 276 (1997) 307–326, https://doi.org/10.1016/S0076-6879(97)76066-X.

[39] A. Morin, B. Eisenbraun, J. Key, P.C. Sanschagrin, M.A. Timony, M. Ottaviano, P. Sliz, Collaboration gets the most out of software, ELife 2 (2013), e01456, https://doi.org/10.7554/eLife.01456.

[40] A. Jurcik, D. Bednar, J. Byska, S.M. Marques, K. Furmanova, L. Daniel, P. Kokkonen, J. Brezovsky, O. Strnad, J. Stourac, A. Pavelka, M. Manak, J. Damborsky, B. Kozlikova, CAVER analyst 2.0: analysis and visualization of channels and tunnels in protein structures and molecular dynamics trajectories, Bioinformatics 34 (20) (2018) 3586–3588, https://doi.org/10.1093/bioinformatics/bty386 (n.d.).

[41] F. Madeira, Y.M. Park, J. Lee, N. Buso, T. Gur, N. Madhusoodanan, P. Basutkar, A. R.N. Tivey, S.C. Potter, R.D. Finn, R. Lopez, The EMBL-EBI search and sequence analysis tools APIs in 2019, Nucleic Acids Res. 47 (2019) W636–W641, https://doi.org/10.1093/nar/gkz268.

[42] R.K. Thauer, Methyl (alkyl)-coenzyme M reductases: nickel F-430-containing enzymes involved in anaerobic methane formation and in anaerobic oxidation of methane or of short chain alkanes, Biochemistry 58 (2019) 5198–5220, https://doi.org/10.1021/acs.biochem.9b00164.

[43] D.D. Nayak, N. Mahanta, D.A. Mitchell, W.W. Metcalf, Post-translational thioamidation of methyl-coenzyme M reductase, a key enzyme in methanogenic and methanotrophic Archaea, ELife 6 (2017), e29218, https://doi.org/10.7554/eLife.29218.

[44] P.T. Lang, J.M. Holton, J.S. Fraser, T. Alber, Protein structural ensembles are revealed by redefining X-ray electron density noise, Proc. Natl. Acad. Sci. U S A. 111 (2014) 237–242, https://doi.org/10.1073/pnas.1302823110.

[45] C.J. Hahn, O.N. Lemaire, J. Kahnt, S. Engilberge, G. Wegener, T. Wagner, Crystal structure of a key enzyme for anaerobic ethane activation, Science 373 (2021) 118–121, https://doi.org/10.1126/science.abg1765.

[46] T. Fransson, R. Chatterjee, F.D. Fuller, S. Gul, C. Weninger, D. Sokaras, T. Kroll, R. Alonso-Mori, U. Bergmann, J. Kern, V.K. Yachandra, J. Yano, X-ray emission spectroscopy as an in situ diagnostic tool for X-ray crystallography of metalloproteins using an X-ray free-electron laser, Biochemistry 57 (2018) 4629–4637, https://doi.org/10.1021/acs.biochem.8b00325.

[47] P. Rabe, J.J.A.G. Kamps, K.D. Sutherlin, J.D.S. Linyard, P. Aller, C.C. Pham, H. Makita, I. Clifton, M.A. McDonough, T.M. Leissing, D. Shutin, P.A. Lang, A. Butryn, J. Brem, S. Gul, F.D. Fuller, I.-S. Kim, M.H. Cheah, T. Fransson, A. Bhowmick, I.D. Young, L. O'Riordan, A.S. Brewster, I. Pettinati, M. Doyle, Y. Joti, S. Owada, K. Tono, A. Batyuk, M.S. Hunter, R. Alonso-Mori, U. Bergmann, R.L. Owen, N.K. Sauter, T.D.W. Claridge, C.V. Robinson, V.K. Yachandra, J. Yano, J.F. Kern, A.M. Orville, C.J. Schofield, X-ray free-electron laser studies reveal correlated motion during isopenicillin N synthase catalysis, Sci. Adv. 7 (2021), eabh0250, https://doi.org/10.1126/sciadv.abh0250.

[48] S.P.J. Albracht, D. Ankel-Fuchs, R. Böcher, J. Ellermann, J. Moll, J.W. van der Zwaan, R.K. Thauer, Five new EPR signals assigned to nickel in methyl-coenzyme M reductase from Methanobacterium thermoautotrophicum, strain Marburg, Biochim. Biophys. Acta 955 (1988) 86–102, https://doi.org/10.1016/0167-4838(88)90182-3.

[49] Y. Zhou, A.E. Dorchak, S.W. Ragsdale, In vivo activation of methyl-coenzyme M reductase by carbon monoxide, Front. Microbiol. 4 (2013) 69, https://doi.org/10.3389/fmicb.2013.00069.

[50] A. Butryn, P.S. Simon, P. Aller, P. Hinchliffe, R.N. Massad, G. Leen, C.L. Tooke, I. Bogacz, I.-S. Kim, A. Bhowmick, A.S. Brewster, N.E. Devenish, J. Brem, J.J.A. G. Kamps, P.A. Lang, P. Rabe, D. Axford, J.H. Beale, B. Davy, A. Ebrahim, J. Orlans, S.L.S. Storm, T. Zhou, S. Owada, R. Tanaka, K. Tono, G. Evans, R.L. Owen, F. A. Houle, N.K. Sauter, C.J. Schofield, J. Spencer, V.K. Yachandra, J. Yano, J. F. Kern, A.M. Orville, An on-demand, drop-on-drop method for studying enzyme catalysis by serial crystallography, Nat. Commun. 12 (2021) 4461, https://doi.org/10.1038/s41467-021-24757-7.

[51] T.W. Johnson, R.A. Gallego, A. Brooun, D. Gehlhaar, M. McTigue, Reviving B-factors: retrospective normalized B-factor analysis of c-ros oncogene 1 receptor tyrosine kinase and anaplastic lymphoma kinase L1196M with crizotinib and lorlatinib, ACS Med. Chem. Lett. 9 (2018) 878–883, https://doi.org/10.1021/acsmedchemlett.8b00147.

SUPPORTING INFORMATION

XFEL Serial Crystallography Reveals the Room Temperature Structure of Methyl-Coenzyme M Reductase

Christopher J. Ohmer[a,j], Medhanjali Dasgupta[b,j], Anjali Patwardhan[a], Isabel Bogacz[b], Corey Kaminsky[b], Margaret D. Doyle[b], Percival Yang-Ting Chen[c,i], Stephen M Keable[b], Hiroki Makita[b], Philipp S. Simon[b], Ramzi Massad[b], Thomas Fransson[d], Ruchira Chatterjee[b], Asmit Bhowmick[b], Daniel Paley[b], Nigel W. Moriarty[b], Aaron S. Brewster[b], Leland B. Gee[e], Roberto Alonso-Mori[e], Frank Moss[e], Franklin D. Fuller[e], Alexander Batyuk[e], Nicholas K. Sauter[b], Uwe Bergmann[f], Catherine L. Drennan[c,g,h], Vittal K. Yachandra[b], Junko Yano[b], Jan F. Kern[b], Stephen W. Ragsdale[a]

[a] Department of Biological Chemistry, University of Michigan Medical School, 1150 W. Medical Center Dr., 5200 MSRBIII, Ann Arbor, MI 48109-0606, USA.

[b] Molecular Biophysics and Integrated Bioimaging Division, Lawrence Berkeley National Laboratory, Berkeley, CA 94720, USA.

[c] Department of Chemistry, Massachusetts Institute of Technology, 77 Massachusetts Avenue, Cambridge, MA 02139, USA.

[d] Department of Theoretical Chemistry and Biology, KTH Royal Institute of Technology, Stockholm, Sweden.

[e] LCLS, SLAC National Accelerator Laboratory, Menlo Park, CA 94025, USA.

[f] Department of Physics, University of Wisconsin-Madison, Madison, WI 53706, USA

[g] Department of Biology and the Howard Hughes Medical Institute, Massachusetts Institute of Technology, 77 Massachusetts Avenue, Cambridge, MA 02139, USA

.[h]Canadian Institute for Advanced Research, Bio-inspired Solar Energy Program, Toronto, ON M5G 1M1, Canada

[i] Current Address: Morphic Therapeutic, 35 Gatehouse Drive, A2, Waltham, MA 02451, USA

[j] These authors contributed equally.

Corresponding authors: Stephen W. Ragsdale, sragsdal@umich.edu; Junko Yano, jyano@lbl.gov; Jan F. Kern, jfkern@lbl.gov

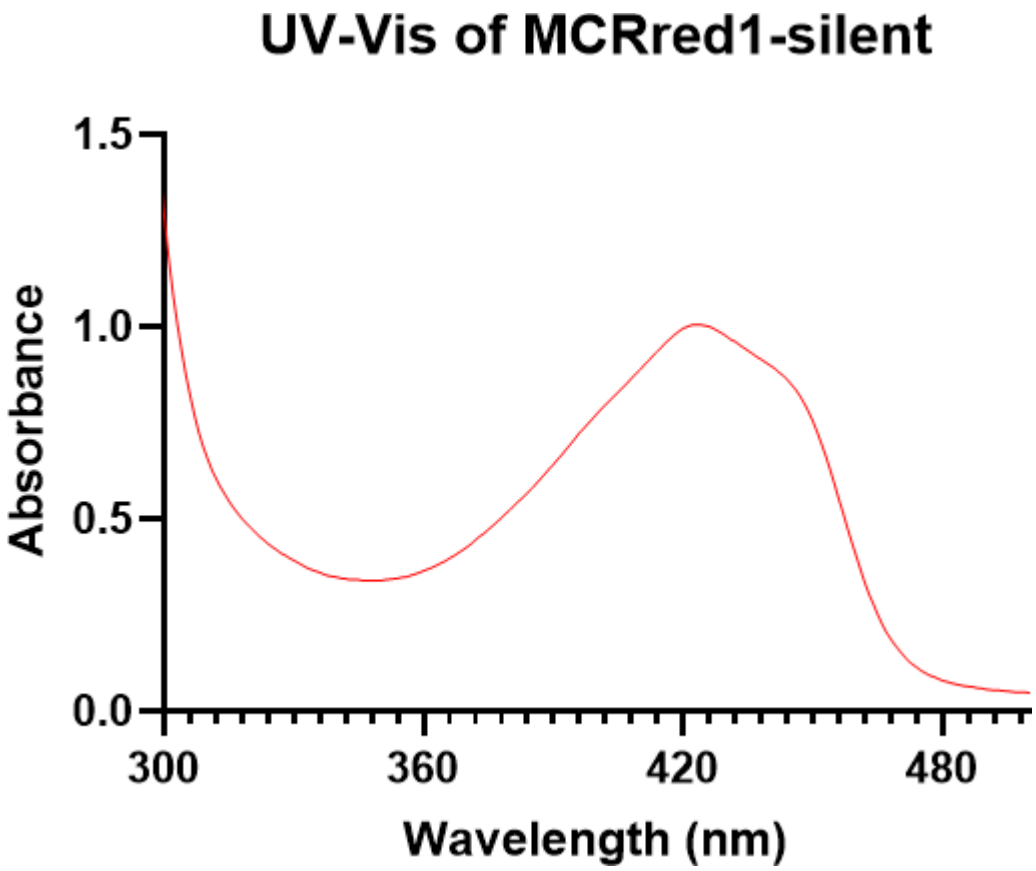

SI Fig 1: UV-Vis spectrum of purified MCR protein shows the Ni(II) absorption at 420nm. Spectrum was measured in 50 mM Tris pH7.6 on a Shimadzu UV-2600 UV-Vis spectrophotometer.

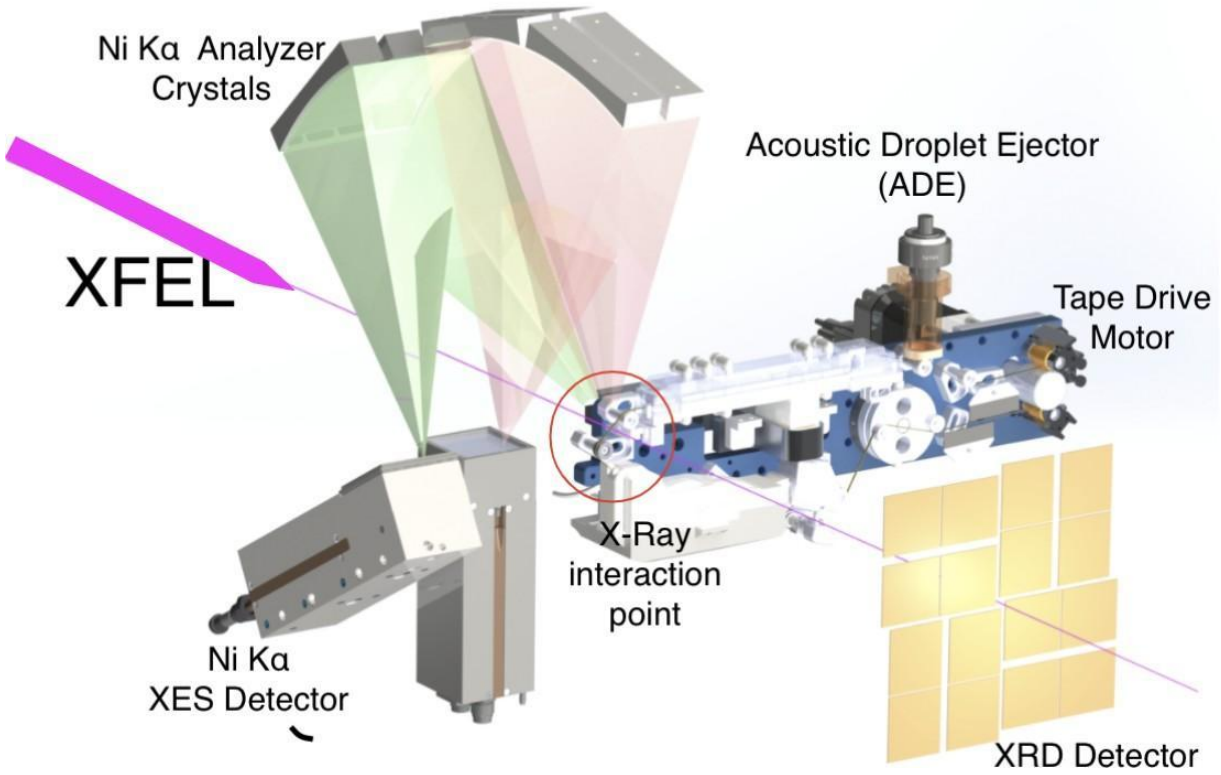

SI Fig 2: A cartoon depiction of our Drop On Tape (DOT) sample delivery setup with simultaneous XRD and XES data collection at MFX, LCLS (SLAC, Menlo Park, CA) enables us to collect both structural as well as metal oxidation state information in MCR *in-crystallo* .Shown in this picture is a two-metal (Ni and Fe) XES setup which permits measurements of both either simultaneously or only one of them without chaining the entire setup, depending on the enzyme system studied (Fe, Ni, or Fe+Ni).

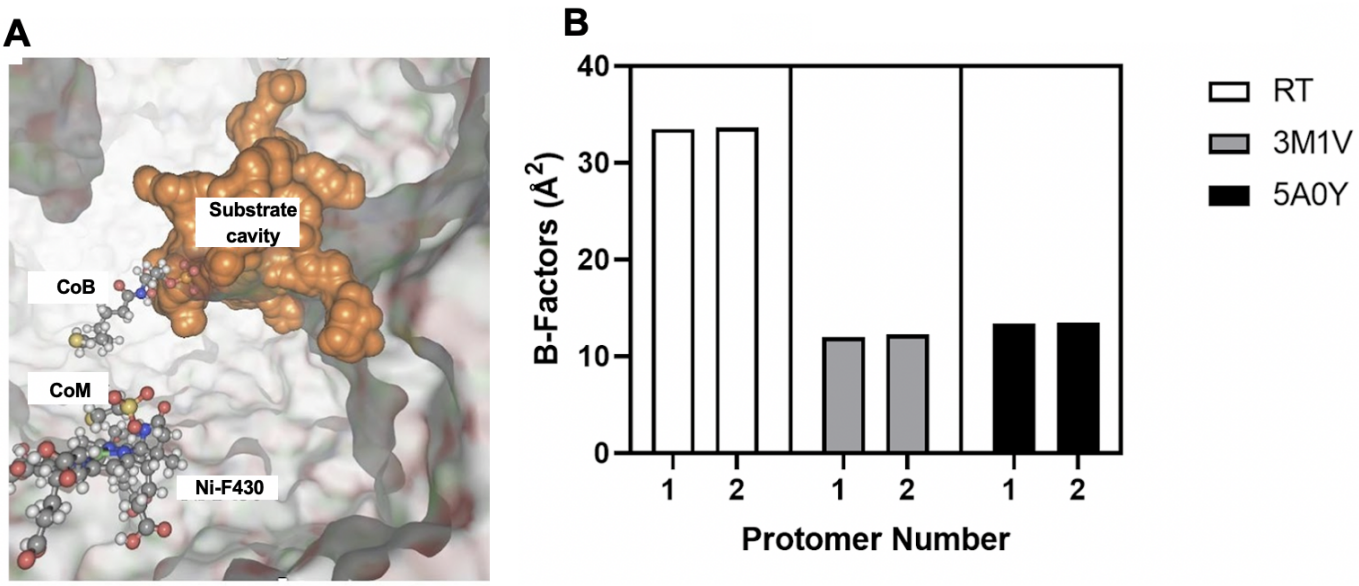

SI Fig 3: (A) Caver [43] cavity analysis shows the substrate channel found in all structures of MCR to date (substrate channel in our RT structure shown as orange surface) in the active site, with the Ni-F_{430} and the CoB and CoM coenzymes shown in ball and stick representation. (B) B factor analysis shows similar flexibilities in both protomers of MCRred1-silent independent of data collection temperatures.

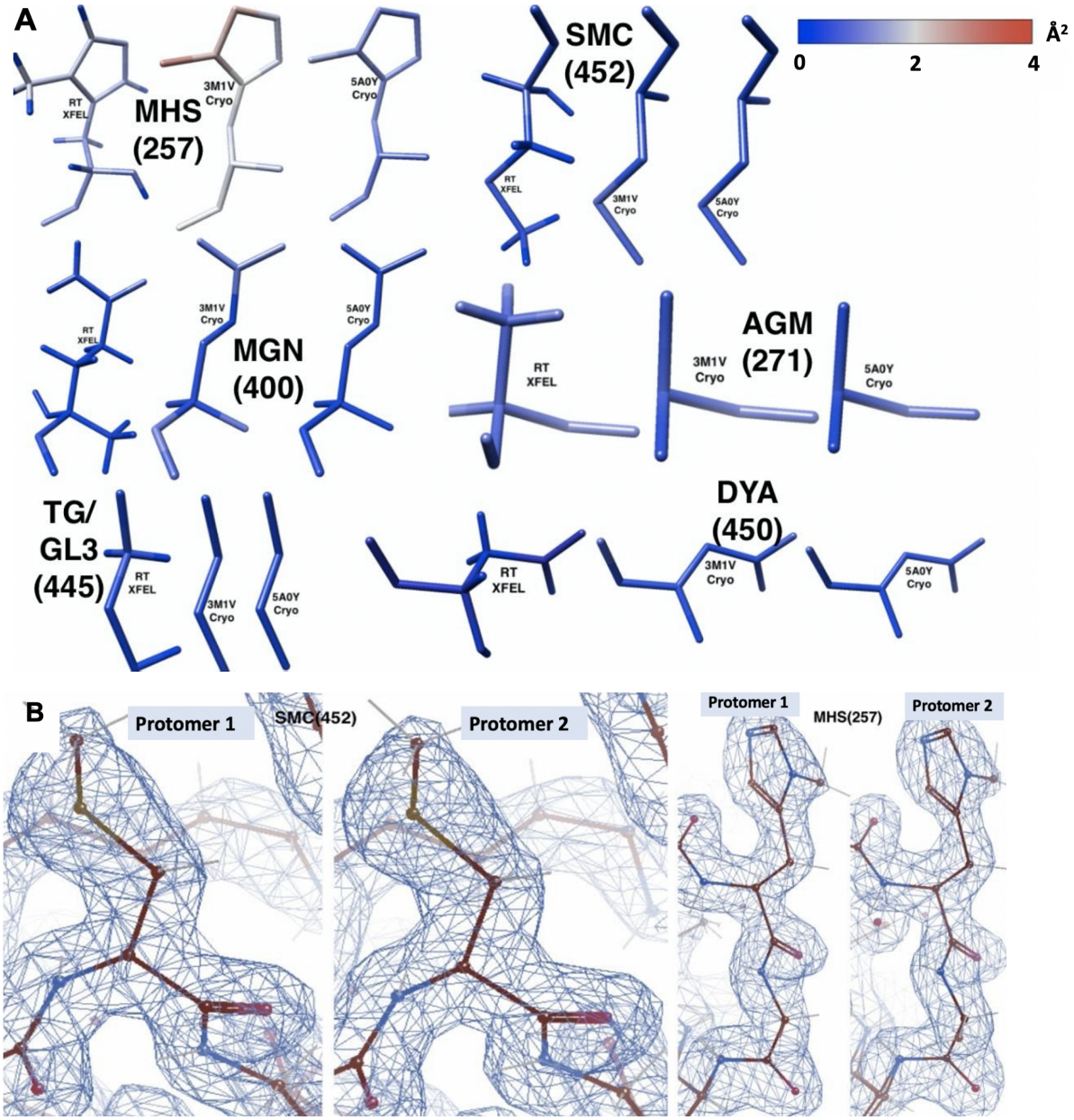
A
RT XFEL
3M1V Cryo
5A0Y Cryo
MHS (257)
SMC (452)
0
2
4
Å²
MGN (400)
AGM (271)
TG/ GL3 (445)
DYA (450)
B
Protomer 1
SMC(452)
Protomer 2
Protomer 1
MHS(257)
Protomer 2

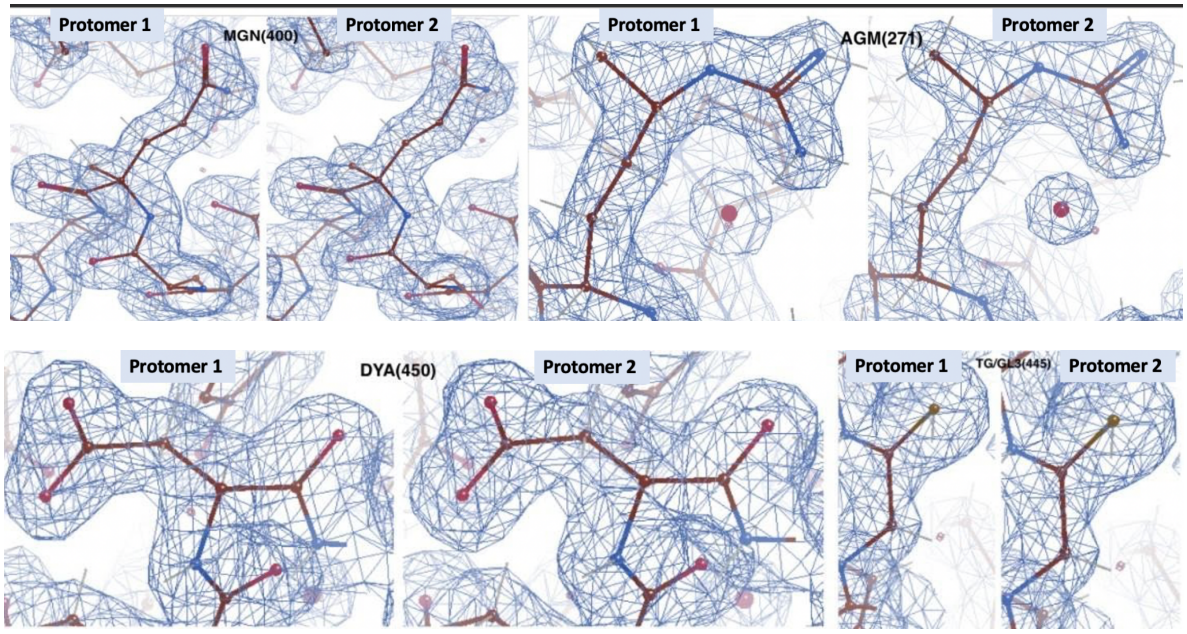

SI Fig 4: (A) From Top Left Clockwise: Modified amino acids, N1-Methylated Histidine (MHS), S-MethylCysteine (SMC), 5-Methyl Arginine (AGM), Di-Dehydro Aspartic Acid (DYA), Thioglycine (TG/GL3), and 2-Methyl Glutamine (MGN), colored by B factors of the individual atoms in MCRred1-silent structures collected at room temperature at SLAC during LCLS beamtime proposal LX45, and under cryogenic temperatures (3M1V,5A0Y). The normalized b-factors were subtracted by the lowest normalized B-factor residue to give normalized B-factors greater than 0 for figure visualization in Chimera and Chimera-X. (B) 2Fo-Fc electron densities for the modified amino acids in our RT MCRred1-silent structure contoured at 1.5 sigma.

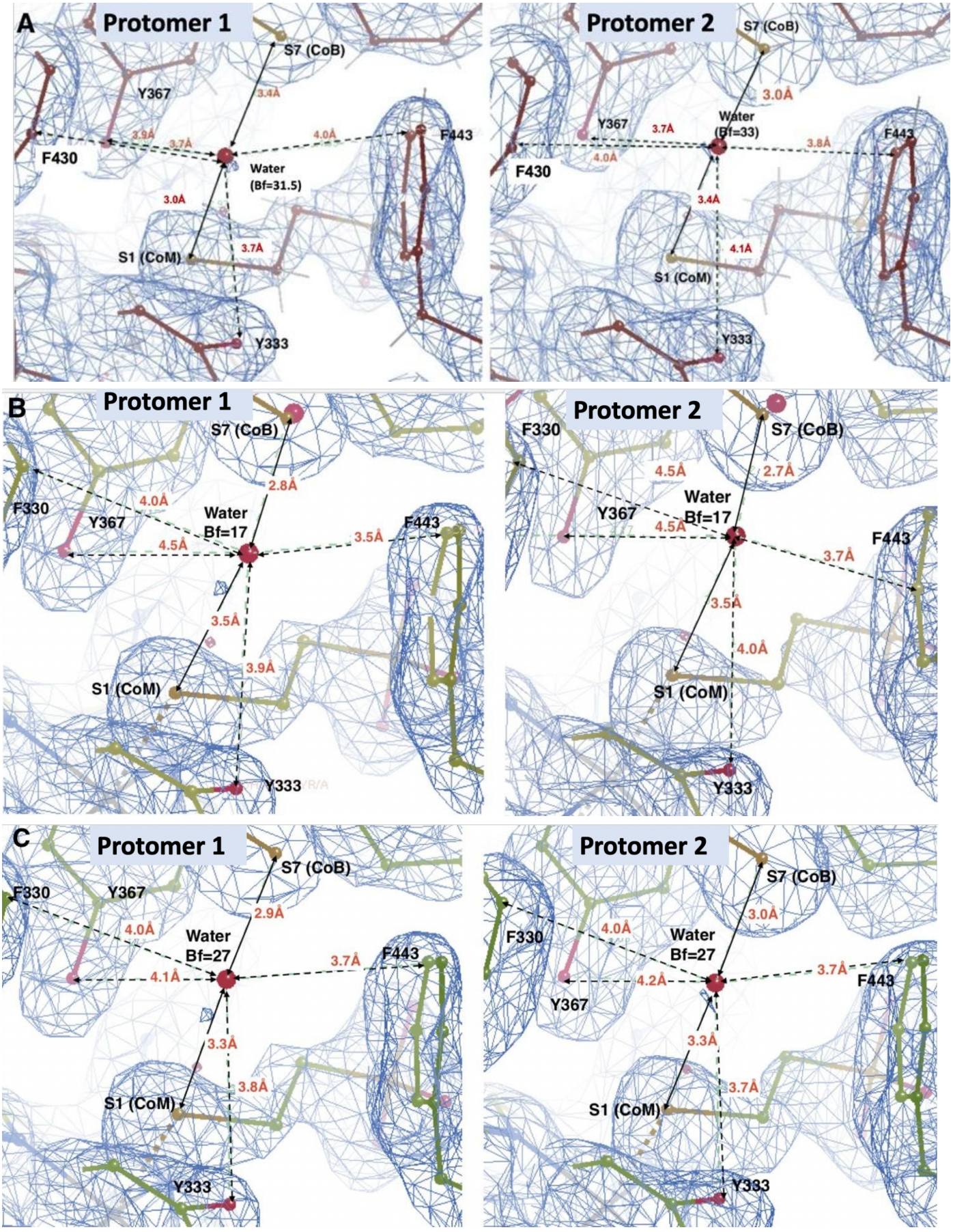
A
Protomer 1
S7 (CoB)
Y367
3.4Å
3.9Å
3.7Å
4.0Å
F443
F430
Water
(Bf=31.5)
3.0Å
S1 (CoM)
3.7Å
Y333
Protomer 2
S7 (CoB)
3.0Å
Y367
3.7Å
Water
(Bf=33)
3.8Å
F443
4.0Å
F430
3.4Å
4.1Å
S1 (CoM)
Y333
B
Protomer 1
S7 (CoB)
2.8Å
F330
4.0Å
Y367
Water
Bf=17
F443
4.5Å
3.5Å
3.5Å
3.9Å
S1 (CoM)
Y333
Protomer 2
F330
S7 (CoB)
4.5Å
2.7Å
Water
Bf=17
Y367
4.5Å
F443
3.7Å
3.5Å
4.0Å
S1 (CoM)
Y333
C
Protomer 1
S7 (CoB)
F330
Y367
2.9Å
4.0Å
Water
Bf=27
3.7Å
F443
4.1Å
3.3Å
3.8Å
S1 (CoM)
Y333
Protomer 2
S7 (CoB)
3.0Å
F330
4.0Å
Water
Bf=27
3.7Å
4.2Å
F443
Y367
3.3Å
3.7Å
S1 (CoM)
Y333

SI Fig 5: 2Fo-Fc density shows up around 1.8 sigma in between MCRred1-silent substrates, CoM and CoB in protomer 1, and around 1.4 sigma for the second protomer. (Distances between water and substrates, CoM and CoB shown as a straight black arrow, distances between nearby amino acid residues shown as dotted arrows). (A) We have modeled a water molecule in that density with 100% occupancy in both protomers (B factor of the water is ~32 $Å^2$) in our RT XFEL structure, indicating this is not a very "mobile" water. These waters seem to be conserved across the MCR cryogenic structures (B, 3M1V and C, 5A0Y), although there are clear differences in the coordination environment of the waters in the respective models.

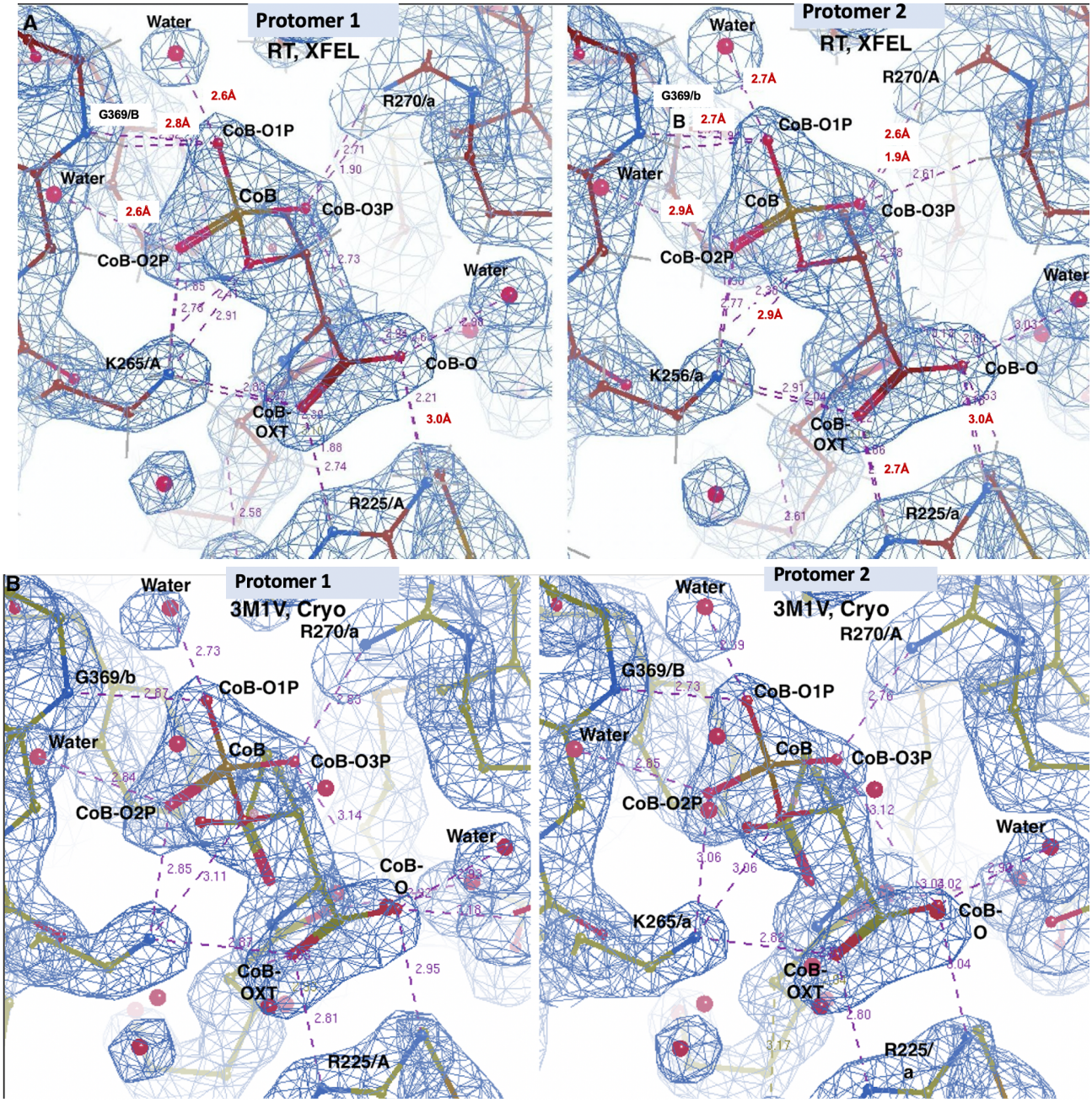
A
Protomer 1
RT, XFEL
Water
G369/B
2.6Å
2.8Å
CoB-O1P
R270/a
Water
CoB
CoB-O3P
2.6Å
CoB-O2P
Water
K265/A
CoB-O
CoB-
OXT
3.0Å
R225/A
Protomer 2
RT, XFEL
Water
2.7Å
R270/A
G369/b
B
2.7Å
CoB-O1P
2.6Å
1.9Å
Water
CoB
CoB-O3P
2.9Å
CoB-O2P
Water
K256/a
CoB-O
CoB-
OXT
3.0Å
2.7Å
R225/a
B
Protomer 1
3M1V, Cryo
Water
R270/a
G369/b
CoB-O1P
Water
CoB
CoB-O3P
CoB-O2P
Water
CoB-
O
CoB-
OXT
R225/A
Protomer 2
3M1V, Cryo
Water
R270/A
G369/B
CoB-O1P
Water
CoB
CoB-O3P
CoB-O2P
Water
K265/a
CoB-
O
CoB-
OXT
R225/
a

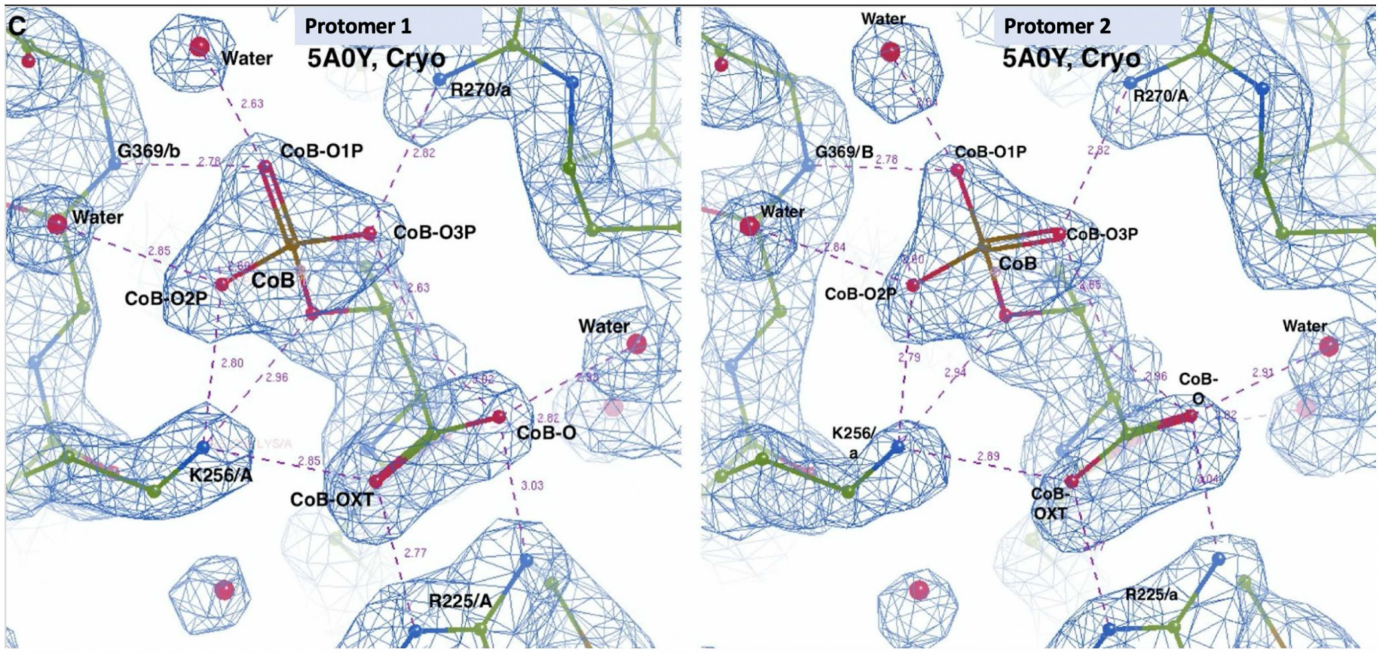

SI Fig 6: Coordination environment of the CoB substrate seems intact in the (A) RT as well as cryogenic (B, 3M1V and C, 5A0Y) MCRred1-silent models, further indicating the "locked" nature of the MCRred1-silent active site, following NiI to NiII oxidation. 2F0-Fc map is contoured at 1.5 sigma.

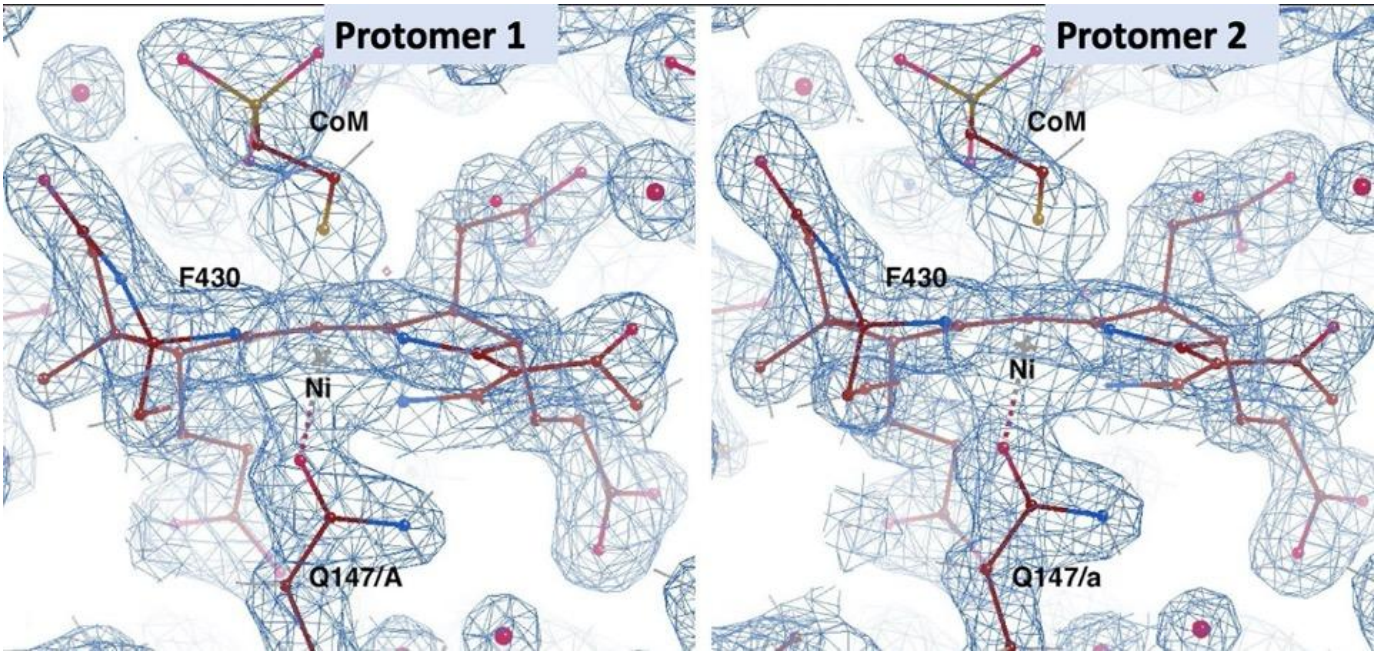

SI Fig 7: Coordination environment of the CoM substrate analog, along with the Ni-F430 cofactor and its coordinating partner, Gln147, shown in our MCRred1-silent models. 2Fo-Fc map is contoured at 1.5 sigma. Figure made in COOT.

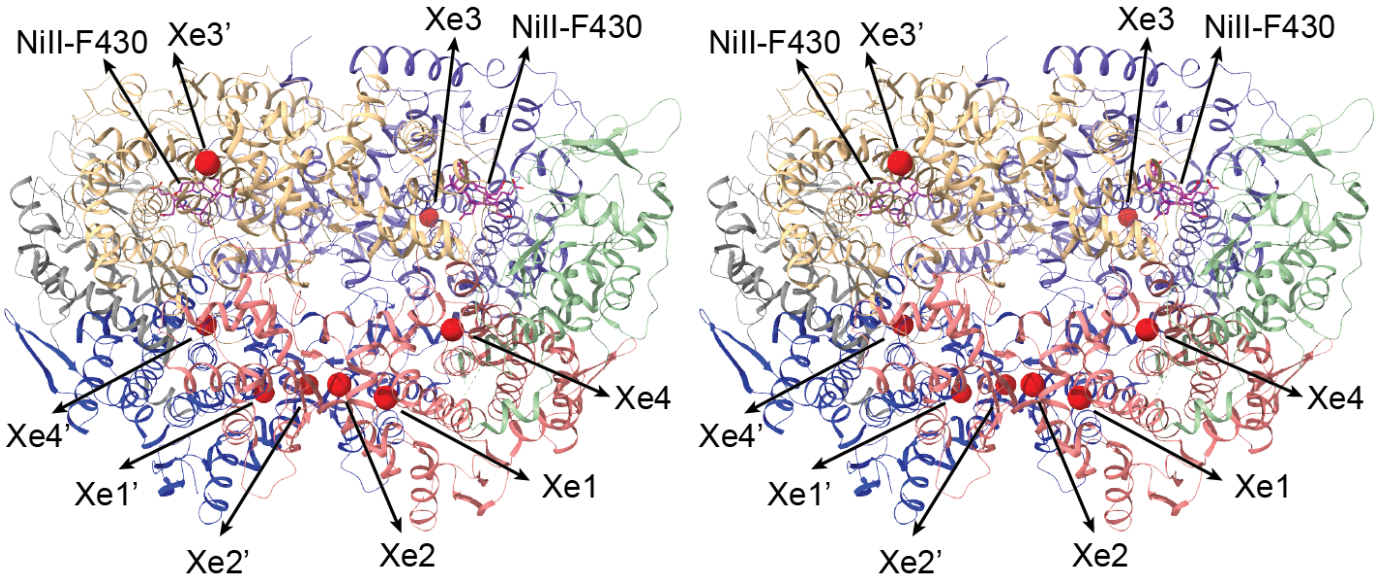

SI Fig 8: Structure of MCRred1-silent Xe pressurized structure shows the location of 4 xenons per trimer. Xe numbering 1,2,3,4 for Protomer 1 and 1`,2`,3` and 4` for Protomer 2. Chain coloring is the same as in Fig 2A. Figure was made with Chimera.

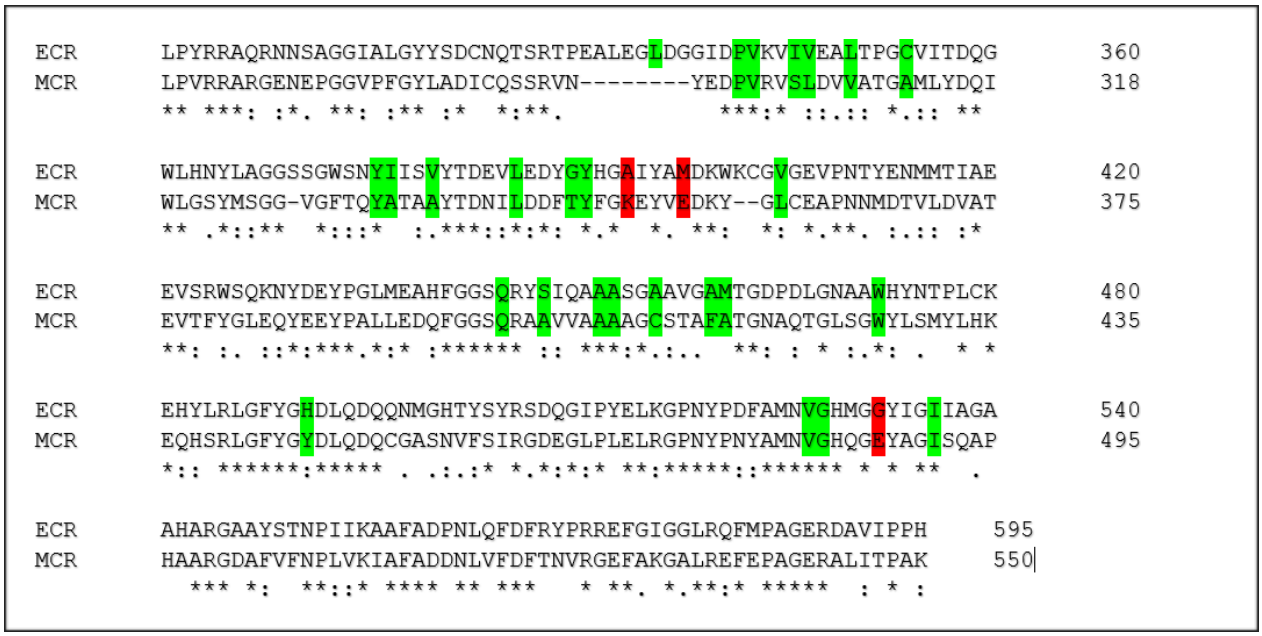

SI Fig 9: Pairwise sequence alignment of Ethyl Coenzyme M Reductase (ECR) (PDB: 7B1S, cryogenic) with our room temperature MCR structure to highlight the differences and similarities between key residues that form a gas tunnel in ECR. Alignments were made with the Clustal-Omega tool from EMBL. Residues in red denote changes between hydrophobic and hydrophilic of aligned structure, while green denotes residues associated with the ECR gas tunnel in Hahn *et.*

SI Table 1: XFEL X-ray Diffraction Data collection at MFX, LCLS (SLAC) and Refinement statistics

Diffraction Parameters	**data collection**	
	date collection temp	300K
	Serial	yes
	diffraction radiation	
	protocol	single wavelength
	diffraction source	
	source type	FEL
	Source details	LCLS MFX
	wavelength	1.300734
	diffraction detector	
	detector	RAYONIX MX340-HS
	detector type	CCD
Serial Measurement	sampling frequency [Hz]	30
	pulse duration [fs]	30
	photon energy [keV]	9.5
	focal spot size [um2]	16
	pulse rep rate [Hz]	30
	pulse energy [uJ]	2200
	collimation	compound refractive lenses
	collection time [h]	0.58
Data Reduction	run numbers	44-53
	total images	73742
	crystal hits	24589
	lattices indexed	22706

Collection Statistics	collection time (mins)	41
	unique reflections	189345
	completeness	99.91
	data redundancy	41.43
	res high	1.9
	CC1/2	0.979
	Rsplit	0.515
	I/s(I)	3.356
Resolution Shells	hig	1.9
	low	1.93
	unique refl	9505
	completeness	99.82%
	redundancy	9.89
	CChalf	0.379
	Rsplit	0.831
	Av I/s(I)	0.696
Softwares used and Refinement stats	data reduction	cctbx.xfel
	data scaling	cctbx.xfel.merge
	phasing	Phenix
	refinement	Phenix
	Rwork	15%
	Rfree	18%
	Ramachandran outliers	4 (0.16%)

SI Table 2: Xe X-ray diffraction data collection statistics and Xe refinement statistics.

	Xe-derivatived MCR-Ni(II)
Beamline	ALS 8.2.2
Space group	$P2_1$
Cell dimensions (Å)	a=82.0, b=115.7, c=123.4, β=92.5
Wavelength (Å)	1.5498
Resolution (Å)	69.6-2.50 (2.59-2.50)
# unique reflections	151627
Completeness (%)	97.1 (95.4)
Redundancy	3.0 (2.9)
$\langle I/\sigma I \rangle$	9.8 (2.3)
R_{sym}	0.086 (0.493)
$CC_{1/2}$	(0.731)
Resolution (Å)	69.6-2.50
# unique reflections	151575
R_{work} (%) / R_{free} (%)	17.8/21.8
RMS bond lengths (Å)	0.002
RMS bond angles (°)	0.531
Average B-factor (Å^2)	39.8
Ramachandran plot	
Favored (%)	97.14
Allowed (%)	2.86
Outliers (%)	0.00
Rotamer outliers (%)	0.30

SI Table 3: Comparing active site distances in the RT XFEL MCRred1-silent with previously collected cryo structures (Reported here only for both protomers, separated by commas).

aSm = sulfur (S1) atom of the CoM moiety of methyl-SCoM bSc = sulfur (S7) atom of the HSCoB moiety	**XFEL RT (Å)**	**Cryo(3M1V) (Å)**	**Cryo (5A0Y) (Å)**
Ni–OE1(Gln147/A)	2.27, 2.28	2.34, 2.31	2.31, 2.30
Ni–aSm	2.40, 2.46	2.44, 2.44	2.44, 2.44
Ni–bSc	8.76, 8.77	8.76, 8.57	8.68, 8.66
02S(CoM)-NH1(Arg120/C)	2.89, 2.83	2.92, 2.88	2.93*, 2.89
OH(Tyr367/B)-aSm	3.03, 3.04	3.11, 3.13	3.1, 3.12
O(CoB)-NE(Arg225/A)	3.79, 3.87	3.91, 3.92	3.87, 3.86
OH(Tyr333/A)-aSm	3.0, 3.14	3.08, 3.08	3.07, 3.09
O(Arg270/A)-NE2(MHS257/a)	7.34,7.16	7.26, 7.21	7.06, 6.97
aSm-bSc	6.4, 6.33	6.16, 6.34	6.26, 6.28
Water -aSm	3.05 , 3.4	3.53, 3.49	3.32, 3.28
Water -bSc	3.29, 2.99	2.64, 2.69,	2.96, 2.93

* Distance averaged over both conformations (A and B) of R120(C) in PDB 5A0Y.